

1 **Cenozoic dextral shearing along the Great Kavir – Doruneh Fault System**
2 **(Central Iran)**

3
4 **Andrea Zanchi¹, Stefano Zanchetta^{1,*}, Fabrizio Berra², Massimo Mattei³, Hamid Reza Javadi⁴**
5 **and Chiara Montemagni¹**

6
7 1: Dipartimento di Scienze dell’Ambiente e della Terra, Università degli Studi di Milano – Bicocca,
8 Milano, Italy

9 2: Dipartimento di Scienze della Terra “Ardito Desio”, Università degli Studi di Milano, Milano, Italy

10 3: Dipartimento di Scienze, Università Roma TRE, Roma, Italy

11 4: Geological Survey of Iran, Tehran, Iran

12

13 * corresponding author: stefano.zanchetta@unimib.it

14

15 **Orcid:**

16 A.Z.: 0000-0001-7190-6131

17 S.Z.: 0000-0001-7690-969X

18 F.B.: 0000-0002-4354-1806

19 M.M: 0000-0001-7800-8764

20 H.R.J.: 0000-0002-2660-6292

21 C.M.: 0000-0002-2850-9744

22

23

24

25 **Key-words:** intracontinental faults, Central Iran, wrench tectonics, transpression, Great Kavir
26 Doruneh Fault System, paleostress

27

28

29

30

31

32

33

34

35 **Abstract**

36 The structural analysis of large intracontinental wrench faults is fundamental for deciphering the long-
37 term evolution of continental crust in complex areas in terms of their geodynamic evolution and large-
38 scale crustal block displacements. In this contribution, we demonstrate a pre-Miocene dextral activity
39 of the present-day left-lateral Great Kavir - Doruneh Fault System (GKDFS, Central Iran), one of the
40 major intracontinental active strike-slip faults extending from the Afghan border to the Nain region
41 between Central Iran and the Sanandaj-Sirjan Zone. We document important dextral shearing
42 recorded along a segment of the GKDFS, the Arusan Fault System (AFS), located east of Jandaq,
43 close to the present-day active trace of the GKDFS. The AFS include several ENE-WSW striking
44 strands exposed for a length of more than 50 km, which couple pre-Cretaceous ophiolites and
45 metamorphic basement units with the Cretaceous succession of the Khur basin. The fault shows
46 transpressional structures consistent with a dextral shear including thrusts and *en échelon* folds
47 affecting the Cretaceous carbonate units. Paleostress reconstruction based on mesoscopic fault
48 analysis and related folds geometry allowed to establish vorticity parameters indicating that
49 deformation occurred close to a total simple shear regime with a calculated W_k between 0.9 and 1.
50 The enormous Meso-Cenozoic dextral displacements occurred along the AFS and along the entire
51 GKDFS are attested by the up to several hundreds of kilometers offset of the Paleotethys suture zone,
52 from NE Iran to the western border of Central Iran.

53

54 **1 Introduction**

55 Strong deformation of continental crust along major wrench faults, resulting from large rotations of
56 crustal blocks along vertical axes, was firstly suggested 50 years ago by Freund (1970) along the
57 Dead Sea Transform. This phenomenon was later documented all over the world (e.g. Ron et al.,
58 1984; Sonder et al., 1994; Storti et al., 2003; Walker & Jackson, 2004; Onderdonk, 2005; Mattei et
59 al., 2015). Wrench tectonics is often responsible for large-scale (several hundreds to thousands of
60 kilometers) displacements of previously continuous geological structures, such as orogens and major
61 suture zones (Storetvedt 1974, 1987; Tapponier et al., 1990). The Permian dextral mega-shear
62 transforming Pangea-A to Pangea-B (Muttoni et al., 2009; Kent & Muttoni, 2020) and the
63 displacement, along the San Andrea Fault of the Baja California Peninsula (e.g. Mount & Suppe,
64 1987) are just some of the many examples of the role played by wrench tectonics in the evolution of
65 continental crust.

66 One of the most fascinating and still unsolved problem of the geodynamic evolution of this area is
67 the enigma of block rotations within the internal portion of Central Iran (Figure 1). Starting from the
68 first ideas of Davoudzadeh & Schmidt (1981) and Soffel et al. (1996), who have suggested a total

69 counterclockwise rotation of 135° of a large part of Central Iran with respect to stable Eurasia since
70 the Triassic, recent works (Mattei et al., 2012, 2015, 2019) confirm that at least some blocks forming
71 the Central Iran area may have rotated counterclockwise up to 80° - 90° since the Jurassic. Evidence
72 of this large-scale block rotations are also based on the displacement of the Paleotethys suture zone
73 in NE Iran. Tectonic units related to the closure of the Paleotethys ocean were displaced from the
74 Mashhad-Torbat Jam area south-westward to the north-western corner of Central Iran (Bagheri &
75 Stampfli, 2008; Zanchi et al., 2009b; 2015; Zanchetta et al., 2013; Berra et al., 2017; Balini et al.,
76 2019) following the trace of the present-day Great Kavir – Doruneh Fault System (GKDFS). The idea
77 of large-scale block rotations within Iran was also proposed by Alavi et al. (1997) and more recently
78 by several authors (Balini et al., 2009, 2019; Zanchi et al., 2009b) to explain similarities between the
79 Aghdarband Triassic succession of NE Iran and the Triassic of Naxhlak, which is located just north
80 of Anarak in Central Iran (Figure 2).

81 Pirnia et al. (2020) argue about large crustal-scale rotations properly suggesting that the ophiolites of
82 Sabzevar and Nain Baft, now located about 400 km from each other, were once part of a unique
83 complex, which was possibly displaced along a precursor of the present-day GKDFS during the
84 Cenozoic. Despite its present-day left–lateral motion, well documented by active tectonics and
85 structural studies (Shabanian et al. 2009; Farbod et al., 2011; Bagheri et al., 2017), the idea that a
86 large dextral displacement could have occurred along the GKDFS fits well also in paleogeographic
87 reconstructions related to the Aptian time interval (Barrier & Vrielynck, 2008). These authors, suggest,
88 in fact, in their maps a dextral motion for the Great Kavir Fault, followed by a Late Cretaceous shift
89 to left-lateral motion. Dextral shearing was also recognized in the central part of the GKDFS, where
90 Tadayon et al. (2017, 2019) document dextral transpression during the early Cenozoic along the
91 Taknar fault system, an important strand of the main fault. A shift from a long lasting right-lateral
92 shearing to a post-Miocene active left-lateral motion was recently documented (Javadi et al., 2013,
93 2015). The accommodated left-lateral displacement is supposed to be of a few kilometers, with less
94 than one kilometer during the Quaternary (Farbod et al., 2011, 2016).

95 In this paper, we present new original data on the post-Cretaceous right-lateral activity of an important
96 ENE-WSW dextral shear zone, here named the Arusan Fault System (AFS), related to the western
97 portion of the GKDFS. The AFS extends east of the town of Jandaq, a few kilometers to the south of
98 the trace of the present day Great Kavir Fault which represents the western segment of the entire
99 GKDFS. We integrate field-based structural analyses with new stratigraphic reconstruction and
100 mapping of the Cretaceous units, which provide a firm evidence of Cenozoic dextral shearing along
101 the precursors of the present-day GKDFS, adding new constraints on the evolution of Central Iran.
102 Combining our new data with previous structural information, we propose a model in which the

103 occurrence of dismembered fragments of the Paleotethys suture originally located in NE Iran and
104 now exposed along the NW border of Central Iran is consistent with a large-scale dextral
105 displacement occurred along an intracontinental fault, the AFS representing a portion of its western
106 sector.

107

108 **2 Geological setting**

109 **2.1 Tectonic setting of Central Iran and surrounding area along the GKDFS**

110 The GKDFS extends more than 700 kilometers from the border in NE Iran with Afghanistan running
111 across the Iranian Plateau up to Nain (Figure 1a-b). This fault system, which shows an arcuate shape
112 roughly trending E-W delimits the internal part of Central Iran, which is generally referred as the
113 Central-Eastern Iran Microplate (CEIM). The CEIM is a very complex and still poorly known area,
114 due to the occurrence of enormous sand deserts covering large part of the region. The CEIM is entirely
115 surrounded by an Upper Cretaceous ophiolitic “ring”, often known as the “coloured mélange” which
116 delimits its most internal part. The ophiolitic ring includes different suture zones, from the Sistan to
117 the East separating the CEIM from the Helmand and Farah blocks of Afghanistan to the Sabzevar
118 ophiolites, which were deformed and emplaced between the end of the Cretaceous and the beginning
119 of the Cenozoic, both showing HP metamorphism (Rossetti et al., 2015; Jentzer et al., 2020). A
120 possible connection between the Sabzevar and the Nain ophiolites bordering the NW corner of the
121 CEIM, both representing the remnants of Neotethys Cretaceous back-arcs, has been recently
122 suggested by Pirnia et al. (2020) based on compositional and geochemical affinities between the two
123 suites. The CEIM consists of three major blocks, the Yazd, Tabas and Lut blocks separated by N-S
124 trending active dextral faults, accommodating active deformation (Figure 1a). These blocks were part
125 of the stable northern margin of Gondwana during most of the Paleozoic, as suggested by the affinity
126 of their thick Paleozoic successions, which closely resemble the units exposed in the Alborz. A
127 Precambrian metamorphic basement of Gondwanan affinity intruded by Cadomian granitoids is also
128 common to the three blocks. During the Mesozoic, after the Cimmerian collision, they were covered
129 by epicontinental seas taking to the deposition of thick carbonate and terrigenous successions
130 (Wilmsen et al., 2015; 2018; 2020) followed by widespread Eocene volcanic activity and a shallow
131 marine to continental succession of Oligocene to Miocene age. Terrigenous continental deposits
132 characterize the post-Miocene sedimentation in the whole area.

133 In spite of these features, pointing to a general stability of the whole Central Iran, late Paleozoic to
134 Triassic active margin units occur south of the GKDFS between Anarak and Jandaq. These units
135 show marked similarities with the complexes which mark the Paleotethys suture in NE Iran along the
136 southern margin of the Turan domain (Bagheri & Stampfli, 2008, Zanchi et al., 2009b, 2015;

137 Zanchetta et al., 2013, 2018). Similar units occur also in the internal part of the CEIM in the Posht-
138 e-Badam area along one of the major dextral faults separating the Yazd from the Tabas block (Bagheri
139 & Stampfli, 2008; Kargaranbafgi et al., 2011).

140

141 **2.2 Geological setting of the Arusan area along the Arusan Fault System (AFS)**

142 The analysed structures (Figures 1 and 2) are exposed 50 kilometers to the east of Jandaq along the
143 southern margin of the Great Kavir Desert, passing across the small oasis of Arusan, which gives the
144 name to this fault system. The AFS consists of several ENE-WSW dextral strike-slip faults which
145 crop out a few kilometers to the south of the active left-lateral Great Kavir Fault. The AFS is
146 continuously exposed for more than 50 kilometers between Mesr and Airekan, flanking the Kuh-e-
147 Kalateh ridge (Figure 3).

148 The oldest rocks in the area belong to a polymetamorphic basement (Early Giurassic) and to an
149 ophiolitic unit, the Arusan ophiolitic mélange (Bagheri & Stampfli, 2008; Torabi, 2009). Ophiolites
150 form an imbricate system of thrust sheets with serpentized peridotites, altered gabbros, metabasites
151 and severely folded marble layers. The ophiolites are tectonically interleaved within the metamorphic
152 basement unit including quartzites, metapelites, gneiss and amphibolites. Undeformed granitoids and
153 pegmatite swarms are exposed along the AFS showing tectonic to intrusive contacts with the
154 surrounding units. Late Jurassic K-Ar ages (158-147 Ma) were obtained on granites from this
155 intrusive complex (Romanko et al., 1979). These units are tectonically juxtaposed onto the Airekan
156 granitic terrain which has given a Precambrian-early Cambrian U/Pb age obtained on a single zircon
157 (549 ± 15 Ma; Bagheri and Stampfli, 2008) and alternatively a revised younger U/Pb Early
158 Ordovician age (483 ± 2.9 Ma) following Shirdashtzadeh et al. (2018). The crystalline basement is
159 discontinuously covered by the Chah Palang Fm., consisting of sandstones and conglomerates derived
160 from the erosion of the underlying units. This unit, deposited between the Late Jurassic and the Early
161 Cretaceous (Wilmsen et al., 2015), forms the base of the “mid” to Upper Cretaceous succession of
162 the Khur Basin (Wilmsen et al., 2015) deposited to the south of the study area, which is part of the
163 Yazd block of Central Iran.

164

165 **3. Cretaceous stratigraphy of the Khur basin (Arusan area)**

166 A deep revision of the local stratigraphic features of the Cretaceous succession of the Arusan area
167 was needed as they differ from those of the central part of the Khur Basin (Wilmsen et al., 2015),
168 which represents our frame of reference.

169 In the Arusan area, the crystalline basement is covered by the siliciclastic deposits of the Chah Palang
170 Fm., discontinuously present at the base of the overlying Cretaceous carbonate succession (Figure

171 4a-b). The Chah Palang Fm. consists of conglomerates and sandstones, with clasts deriving from the
172 underlying basement. The upper part of the unit is finer and richer in quartz grains, documenting a
173 gradual increase in maturity. This siliciclastic unit likely filled depressions in the basement,
174 smoothing the previous topography before the marine transgression marking the rapid and widespread
175 deposition of Cretaceous carbonates in Central Iran. The thickness of the unit is extremely variable,
176 from absent or reduced to a few centimetres sandstones and fine-grained conglomerates to more than
177 200 m. The unit is conformably covered by the Shah Kuh Fm. (Figure 4b), consisting of bioclastic
178 limestone rich in orbitolinids and, locally, rudists, non-conformably laying on basement units. This
179 unit is extremely continuous and characterized by a typical reddish alteration colour, with a thickness
180 ranging from 80 up to 145 m. Locally, the upper part is faintly bedded, marked by hybrid limestones
181 containing well-rounded quartz grains up to 1-2 cm in size, associated with marls and marly
182 limestones, rich in orbitolinids and large bivalves. It is covered, with an erosional base, by red
183 conglomerates with carbonate and basement clasts, passing laterally to sandstones and hybrid
184 limestones, from about 50 to 90 m thick (Figure 4a). Due to its lateral and vertical variability, this
185 interval cannot be easily referred to the Bazyab and Debarsu fms. of the Khur Basin. This unit is
186 thinner with respect to the succession to the south (Wilmsen et al., 2015), and characterized by a
187 coarser grain size, suggesting deposition close to the border of the basin.

188 The massive carbonates of the Haftoman Fm. follow up-section (Figure 4a-b). They are made of
189 siliciclastic limestones with quartz pebbles at the base. They usually display a light gray color and
190 are purely carbonate in the upper part, where rudists are abundant. The unit is from 50 to about 85 m
191 thick. The top of the Haftoman Fm. records a rapid drowning, with deposition of alternating
192 limestones and marls, locally glauconitic. The succession above the Haftoman Fm. corresponds, for
193 stratigraphic position, to the Farokhi Fm. of the Khur basin (Wilmsen et al., 2015). In the Arusan
194 area, above a transitional unit with 80 m of well-bedded limestones, about 50 m of marls occur with
195 intercalations of limestone beds and lenses, rich in orbitolinids and bivalves. These are covered by
196 ca. 100 m of cherty limestones. A second marly horizon (about 50 m) with abundant zoophycos, with
197 thin intercalations of bioclastic and cherty limestone containing glaucony follows and is covered by
198 cherty limestones that likely contain the Cretaceous-Paleocene boundary (Figure 4c). Typical facies
199 of these units exposed around Arusan are shown in Figure 4 (d - j).

200

201 **4. Structural analyses**

202 **4.1 Methods**

203 In order to characterize the geological and especially structural setting of the area crossed by the
204 Arusan Fault System, our field analyses resulted in a general map (Figure 3) and two detailed original

205 maps (Figures 5 and 6). We integrated our field observation with the analysis of Aster colour
206 composite images and Google Earth detailed imagery (11-11-2013 views).

207 The Arusan Fault System (AFS) consists of several dextral strike-slip fault strands running along the
208 slopes of the Kuh-e-Kalateh (Figures 3, 5 and 6), tectonically coupling the Cretaceous successions
209 with the metamorphic basement and ophiolites. Tectonic slices of Mesozoic pinkish granitoids are
210 exposed along the main fault, which runs to the NE of Kuh-e-Kalateh, passing across the village of
211 Arusan and south of Mohammad Abad reaching Airekan within the Great Kavir desert (Figures 3 and
212 6). The fault trace can be followed from satellite images and available maps for more than 50
213 kilometers. Another important branch of the AFS, occurs west of Arusan, bordering the nameless
214 reliefs (1435 m a.s.l.) exposing the Cretaceous cover; this branch of the fault system joins the main
215 fault just west of Arusan with an overall lateral extension of about 15 kilometers (Figure 3).

216 Dextral faults with a comparable multi-kilometer linear extension also occur along the SE slopes of
217 the Kuh-e-Kalateh close to the Naqi Spring (Figure 3), uplifting the metamorphic basement and the
218 Chah Palang Fm. forming in-line anticlines within the Cretaceous carbonates.

219 We performed mesoscopic structural analyses in about 40 measurement stations located along the
220 main tectonic structures. We measured several hundreds of fault planes with their slickensides,
221 establishing the relative sense of motion through kinematic indicators as growth fibres, Riedel
222 fractures, SC cleavage, etc. (Petit & Barquins, 1998). Folds and cleavages were also analysed in order
223 to analytically evaluate their cylindricity and determine β fold axes.

224

225

226 **4.2 The eastern branch of the Arusan Fault System (E-AFS)**

227 This segment of the AFS is clearly visible on Google Earth satellite images (Figure 5), juxtaposing a
228 thick sandstone succession of the Chah Palang Fm. to the Arusan ophiolites and metamorphic
229 basement. Elongated horses of Mesozoic granites extending for several kilometers occur along the
230 fault, which shows a persistent vertical downthrown of at least some hundred meters relative to the
231 SE block.

232 In the southern portion of the investigated segment (stop I14-22: Figure 3), ENE-WSW to NE-SW
233 dextral faults are associated to conjugate NW-SE left lateral faults and other secondary fractures
234 affecting massive pinkish granitoids (I14-22); in a few stops the main right-lateral fault set is
235 displaced by later normal faults showing throws up to a few meters (I17-5, I17-6).

236 We performed detailed analyses especially to the south of Arusan, mapping the area in order to extend
237 our observations to the macroscale (Figure 5), based on new data on the stratigraphic setting. Here
238 we observed a complex association of strike-slip, oblique-reverse and normal faults related to a large

239 dextral fault zone with a maximum thickness ranging between 100 and 150 m. The AFS displays here
240 an anastomosed pattern (stops I14-6, I15-1, 15-2, 15-21, 15-22, 17-1), characterized by dextral
241 motions on subvertical fault planes with both slight normal and reverse oblique components (pitch
242 up to 35°) and subordinate reverse oblique motions forming a flower structure (Figure 7, section A-
243 A'). The fault zone consists of several vertical horses tens of meters thick, including the quartzite
244 basement, large portions of the Mesozoic granitoids, and the Chah Palang Fm., which are tectonically
245 coupled with the carbonates of the Shah Kuh Fm. along a dextral reverse SE-dipping shear zone
246 showing an up to five meters thick fault core with coarse-grained foliated cataclasites. A cleavage
247 related to SC shear bands formed all along the fault zone.

248 The high-angle oblique fault zone passes southward to a thrust plane (Figure 7, section B-B') stacking
249 the quartzite basement onto the upper part of the Shah Kuh Fm. (Figure 8), thus causing a tectonic
250 repetition of the lower part of the Cretaceous succession (Figure 7, section B-B'). The contact
251 between the basement and the Shah Kuh Fm. in the thrust hanging wall is also faulted showing thin
252 tectonic slices of the Chah Palang Fm., which has been tectonically elided. The hanging wall of the
253 thrust consists of a reduced succession, in which the carbonates of the Shah Kuh directly grade to
254 bioclastic massive limestone of the Haftoman Fm. with a few intercalations of hybrid calcarenite and
255 calcirudite beds containing siliceous clasts (Figure 9a). The basement horse thins out southward, its
256 displacement being accommodated by a thrust plane propagated within the Shah Kuh Fm. of the
257 lower unit forming an additional horse (Figure 7, section C-C'). Both thrust planes stop against a
258 transversal NW-SE left lateral tear fault. SW of this fault the thrust surface is shifted into an upper
259 structural position along the marly layers which separate the Shah Kuh from the Haftoman Fm.
260 (Figure 7, section D-D'), dying out progressively to the SW along the north side of the Kalateh ridge.
261 Regularly spaced left-lateral faults with a horizontal separation of a few hundred meters and normal
262 faults with a WNW-ESE strike (I15-24, I15-25), geometrically consistent with a dextral shear along
263 the master fault (Figure 8b), displace the Cretaceous units in the hanging-wall, sharply stopping
264 against the master fault, which crosscuts all these secondary structures (Figure 7, section B-B').

265 Around the village of Arusan, the fault shows dextral strike-slip kinematic indicators (stop I14-6)
266 along the contact between reddish granitoids and the Farokhi Fm. Altered pseudotachylyte veins
267 occur just to the south of Arusan in the granites along NE-SW dextral faults related to the main system
268 (stop I14-5). The occurrence of cohesive cataclasites, suggest that deformation started at some
269 kilometers of depth.

270 The eastern portion of the fault is poorly exposed south of the oasis of Mohammad Abad (Figures 2
271 and 3), where the metamorphic basement and the Mesozoic granitoids are tectonically coupled with
272 the Chah Palang Fm. The contact is covered with recent deposits and we observed secondary faults

273 trending between ENE-WSW to ESE-WNW with a dextral displacement based on *en échelon* veins
274 (stops I15-31, I15-32; Supplementary Figure 1). In this area, as well, part of the contact between the
275 Chah Palang Fm. and the overlying carbonates of the Shah Kuh Fm. consists of a low-angle fault with
276 a reverse slip based on cleavage orientation (stop I15-33, Supplementary Figure 1).

277

278 **4.3 The western segment of the Arusan Fault System (W-AFS)**

279 Another important fault zone develops to the WSW of Arusan along the southern contact between
280 the crystalline basement and the Cretaceous cover (Figures 3 and 6). The fault zone, which is
281 markedly oblique to the structures of the basement, joins the main branch of the AFS at Arusan,
282 following an ENE-WSW strike. The fault zone is delimited by two parallel faults dipping to the north
283 (Figure 6). The southern one follows the contacts between the cover and the basement, whereas the
284 northern one propagated inside the cover, separating the high strain deformation zone from a poorly
285 deformed block to the north, which shows a continuous Cretaceous stratigraphic succession directly
286 covering the Jandaq metamorphic basement. The fault system produces a lens-shaped deformation
287 zone large about 200-300 meters with NE-SW trending *en échelon* folds (Figure 6; stops I15-10, I15-
288 18, I15-29-35-36), isolated folds trending NE-SW to NNE-SSW (stops I15-13, I15-37) and small
289 thrusts forming two small klippen in the Shah Kuh and Haftoman fms., with disharmonic folds below
290 the thrust planes (Figure 9c,e).

291 In spite of the marked transpressional character of the fault zone indicated by the occurrence of fold
292 and thrust structures, mesoscopic fault populations mainly record dextral motions with a small
293 oblique normal component (stops I15-9, I15-11, 15-15 15-37, Figure 6), or both oblique normal and
294 reverse motions (stops I15-12, I15/16/17, Figure 6). This kinematic features result in the lowering of
295 the Cretaceous succession of the hanging wall with respect to the basement.

296 Variably oriented normal faults (stops I14-30, I15-19/20, I15-26/27, I15-35/36/37; Figure 6) are often
297 superposed on the strike-slip system all over the area. ESE-WSW normal faults with displacements
298 limited to a few meters, geometrically consistent with a dextral shear, occur also in the hanging wall,
299 the largest one varying progressively from west to east into a dextral fault (stop I15-37, Figure 6).

300

301 **4.4 The Naqi Spring Fault**

302 The SE strand of the AFS runs along the eastern slope of the Kalateh Ridge in the area of the Naqi
303 oasis (Figure 3). Here the metamorphic basement and the Chah Palang Fm. are uplifted among the
304 carbonates of the Shah Kuh and Haftoman fms. along NE-SW trending strike-slip faults. The Chah
305 Palang Fm. is severely deformed (I15-7, Figure 3 and Supplementary Figure 1) with SE-verging
306 asymmetric inclined folds (Figure 9d). South of Naqi, similarly to what described along the eastern

307 segment of the AFS, a small klippe of highly fractured and dismembered Shah Kuh Fm. overlies the
308 Chah Palang deformed sandstones in the middle of the valley forming an isolated relief (Figure 9d).
309 The klippe is likely related to a detachment developed between layers with a different rheology given
310 by the underlying folded thin-bedded sandstones and the overlying massive carbonates. Strike-slip
311 faults follow the marly layers of the Farokhi Fm. as suggested by their progressive closure (Figure
312 4c).

313

314 **5. Paleostress versus strain analyses and structural evolution**

315 **5.1 Methods**

316 Selected fault populations were analysed in terms of paleostress determinations (Angelier, 1990;
317 Delvaux & Sperner, 2003 and ref. therein). This technique allows to establish the compatibility among
318 faults showing complex geometry and kinematics, as well as to distinguish fault populations related
319 to different tectonic stages based on rational numerical criteria. Paleostress reconstruction has been
320 applied in several areas of Iran helping to define its complex evolution (Navabpour et al., 2007; Javadi
321 et al., 2013, 2015; Jentzer et al., 2017, Zanchi et al., 2006; 2009a; 2016), ensuring significant results
322 in areas characterized by complex strain patterns related to transpressional and contractional regimes.
323 Results are especially relevant when measured faults are related to small and homogeneous
324 displacements showing a pure shear coaxial deformation. We refer to Angelier (1984, 1990, 2002)
325 and to Delvaux and Sperner (2003) for theoretical principles of the method and adopted algorithms.
326 Paleostress reconstruction was performed in eleven sites (Figures 10 and 11), in which a sufficient
327 number of striated fault planes occurs. Results of inversion in terms of the obtained reduced stress
328 tensor are reported in Table 1. We also prepared rose and Frolich diagrams in Wintensor to synthesize
329 the geometrical features of the measured faults.

330 We used fold data for strain analyses considering geometrical relationships between fault zones,
331 cleavage and folds to determine vorticity parameters, which help to evaluate quantitatively the
332 dominant tectonic regime along the studied strike-slip zones. Transtensional and transpressional shear
333 zones are the result of a simultaneous combination of simple shear and pure shear (Fossen et al.,
334 1994) and can be expressed by the dimensionless kinematic vorticity number W_k (Truesdell, 1953)
335 for any kind of flow. W_k , defined as the relative rate of stretching to rotation (Fossen & Tykoff, 1998),
336 varies between 0 for pure shear and 1 for simple shear (Means et al., 1980). Based on the orientation
337 of the Instantaneous Stretching Axes (ISAs) with respect to the shear zone boundary indicated by the
338 θ angle (Fossen et al., 1994), transtension ($\theta > 45^\circ$) can be separated by transpression ($\theta < 45^\circ$). In
339 addition, Fossen and Tikoff (1993) defined two types of transtension and two types of transpression:
340 wrench (simple shear)-dominated and pure-shear dominated.

341 After calculating paleostress axes, since as reported by Weijermars (1991), the ISAs can be linked
342 under certain conditions to the principal stress axes, we measured the angle θ between the σ_3
343 (corresponding to the ISA_1) in the horizontal plane and the fault zone boundary (Figure 12a). As we
344 have considered that strain increments were infinitesimal the maximum ISA (ISA_1) corresponds to
345 the direction of minimum stress axis (σ_3). The relationships between the ISA_1 and the shear zone
346 boundary are related to the kinematic vorticity number W_k (Figure 12; Fossen & Tikoff, 1993; Fossen
347 et al., 1994; Fossen & Tykoff, 1998) by the equation $W_k = \cos(90^\circ - 2\theta)$, suggested in Fossen and
348 Cavalcante (2017).

349 In transpressional and transtensional zones, linear as well as planar markers rotate during progressive
350 deformation (Fossen et al., 1994) due to the contribution of pure and simple shear components. This
351 applies both for pre-existing markers and for those that form during deformation. Such structures
352 comprise, among others, also fold axes, which rotate depending on the W_k of deformation.

353 Therefore, using the software ArcGIS (esri©), we measured the angle λ between the trend of the fold
354 axes and the shear zone boundary (Figure 12b) assuming that any rotational incremental strain
355 occurred during deformation and that orientation of fold axes is parallel to ISA_1 (Fossen et al., 1994;
356 Tadayon et al., 2019).

357 The results of field-based geological observations, fault and fold analyses, paleostress inversion and
358 strain analyses, were integrated to reconstruct the relative chronology among the studied structures.
359 We suggest the occurrence of two main different deformation stages, which can be related to the
360 Cenozoic evolution of this portion of Central Iran.

361

362 **5.1 Stage 1: NW-verging thrust stacking**

363 This event largely affects the crystalline basement of the area. The contacts among the Arusan
364 ophiolites, the metamorphic basement and the Mesozoic granitoids generally consist of dip-slip SE-
365 dipping reverse and thrust faults forming a NW-verging thrust fan. Fault populations characteristic
366 of this stage (Figure 10) are related to internal stacking among the serpentinite bodies of the Arusan
367 ophiolites (Figure 9e) and the different units of the metamorphic basement. Faults inversion at stop
368 I13-12 (Figure 10a), which is fully representative of this stage, shows a pure compression with a
369 horizontal NW-SE σ_1 and a vertical σ_3 . Fault planes are superposed on previous brittle-ductile shear
370 zones with the same dip, dip-direction and kinematics, suggesting a continuous evolution from ductile
371 to brittle conditions. This is suggested by a down-dip orientation of the stretching lineation on
372 mylonites developed along these shear zones and by their top-to-NW shear sense (Figures 9e and
373 10b). Field relationships among fault population show that these thrust zones (Figure 10a-c) are

374 crosscut by ENE-WSW dextral faults (Figure 10d), which are related to the successive deformation
375 stage.

376

377 **5.2 Stage 2: NE-SW dextral shearing**

378 Most of the fault populations and folds measured within the Cretaceous units refer to this event, which
379 corresponds to the activation of the Arusan Fault System with a dextral shear sense. This stage
380 (Figures 10d and 11) is characterized by a predominance of NE-SW right-lateral fairly pure strike-
381 slip faults often conjugate to NW-SE left-lateral strike-slip faults resulting in a horizontal σ_1 trending
382 from WNW-ESE to a dominant NW-SE trend, a horizontal σ_3 and consequently in a vertical σ_2 . At
383 stop I15-15, along the western termination of the western segment of the AFS, we observe a vertical
384 σ_1 and a horizontal NE-SW trending σ_3 possibly due to stress axes permutation between σ_1 and σ_2
385 along this part of the structure, which shows a significant normal throw of the hanging-wall.

386 Relevant paleostress determinations were obtained for the faults measured along the two main
387 segments of the AFS and are broadly coherent all across the study area. The one exception is given
388 by the small thrust faults measured close to the Naqi Spring (stop I15-7; Supplementary Figure 1),
389 which suggest an E-W pure compression, probably related to local strain partitioning or variations in
390 the paleostress orientation.

391 Complex relationships among the strike-slip Arusan Eastern Fault and thrust faults occur SW of
392 Arusan, where the basement and the base of the Cretaceous cover are thrust on the lower part of
393 the Cretaceous succession, forming a double to triple tectonic repetition of the Shah Kuh Fm (Figure
394 8). As observed in the field, the main thrust surface is crosscut by both dextral and left lateral faults.
395 This suggests that it can be related to the NW-SE compression observed within the basement, or,
396 alternatively, to the first stages of the growth of the AFS, forming a restraining bend, which was later
397 crosscut by the high angle NE-SW dextral faults. A transpressional character of the deformation is,
398 in fact, evident along both segments of the AFS. The western segment shows as well a marked
399 transpression in its central part, which is characterized by *en échelon* fold trains and small thrusts.
400 Normal faults with ESE-WNW also occur in the hanging wall of both faults suggesting a complex
401 triclinic strain pattern (Diaz-Azpiroz et al., 2014). We also observed other small normal faults with
402 variable orientations, which can be related to a younger stage.

403 Geometrical relationships between the trace of shear zone boundaries and the orientation of σ_3
404 obtained with paleostress analyses allowed us to determine vorticity parameters (Figure 12): our data
405 suggest a wrench dominated regime (Figure 12a; Fossen & Tikoff, 1993; Fossen et al., 1994) for both
406 the Arusan Western Fault ($Wk = 0.95-1.0$) and the Arusan Eastern Fault ($Wk = 0.90-1.0$) shear zone
407 (Figure 12a).

408 For the Arusan Western Fault shear zone, in which isolated and *en échelon* folds occur, we obtained
409 a pure shear dominated transpression (Figure 12b), suggesting that first stages of deformation were
410 accommodated by folding. After this first folding stage, deformation shifted along newly formed
411 faults, as suggested by paleostress reconstruction.

412

413 **6. Discussion**

414 **6.1 Comparison with the evolution of the GKDFS**

415 The idea that the GKDFS might be a major structure inherited from the Mesozoic evolution of Central
416 Iran and related to the opening of the Sabzevar Ocean was firstly suggested in the paleogeographic
417 maps published by Barrier and Vrielynck (2008) and later by Morin et al. (2018). These
418 authors proposed an older dextral shearing related to the opening of the Sistan-Sabzevar Ocean
419 followed by inversion of the shear sense at the end of the Cretaceous that led to the closure of the
420 basin. Structural observations of the central and western portion of the GKDFS based on mesoscopic
421 fault associations and displacements observed from satellite images document an important dextral
422 transpression preceding the post-Miocene left-lateral motion (Javadi et al., 2013, 2015). They suggest
423 that dextral motion was active between Eocene and late Miocene with an estimated displacement of
424 280 kilometers evaluated from the Cenozoic counter clockwise (CCW) 35° block rotation of the
425 CEIM identified by Mattei et al. (2015).

426 Evidence of an early activity of the GKDFS accommodating NW-SE directed compression was
427 reported in several areas along the fault trace and adjacent areas. The thrust fan dismembering the
428 Anarak Metamorphic Complex (Bagheri & Stampfli, 2008, Zanchi et al., 2009b, 2015), stacking the
429 Carboniferous accretionary wedge within the Cenozoic succession, was interpreted as an expression
430 of the SW termination of the dextral fault zone (Javadi et al., 2015). In addition, the dextral
431 transpressional structures north of Doruneh, related to *en échelon* folds and to the north of the Taknar
432 Fault, were interpreted as a pre-Pliocene right-lateral imbricate fan (Javadi et al., 2013).

433 A multi-stage evolution of the GKDFS was documented also for its central segment (between
434 Doruneh and Kashmar, Figure 1). Structural, stratigraphic and thermochronological data all point to
435 a polyphase history of the fault (Tadayon et al., 2017, 2019). The provided tectono-stratigraphic
436 evolution includes a first stage of thrust stacking of the ophiolitic units accompanied by the inversion
437 of the Late Cretaceous normal faults bounding the Sabzevar oceanic basin under a NW-SE directed
438 shortening. In this interpretation, shortening resumed at the end of the Eocene, following the same
439 NW-SE direction of compression accompanied by E-W dextral shearing causing the activation of a
440 dextral contractional stepover in the Taknar region, which was followed by a steady-state continuous
441 growth of the structure (Tadayon et al., 2019). North of Kashmar, NE-SW oriented, NW-dipping dip-

442 slip thrust faults stacked the Permian and Cretaceous successions onto the Eocene and were crosscut
443 by almost pure strike-slip E-W trending dextral faults (Tadayon et al., 2017).

444 The precursors of the GKDFS post-date subduction in the Sabzevar region, as testified by the age of
445 magmatic rocks that intruded blueschists-bearing metamorphic units related to the Sabzevar
446 subduction accretionary wedge (Rossetti et al., 2015).

447 A change in the stress regime from a NW-SE to a N-S direction of compression occurred in both
448 areas around the Miocene-Pliocene transition, causing a dramatic change in fault kinematics, with the
449 shift of the GKDFS to a left-lateral transpressional system (Tadayon et al., 2017, 2019).

450 The evolution of the AFS, here reconstructed for the first time, displays an evolution that is broadly
451 similar to the one of the GKDFS. A first stage of NW-SE directed compression activating NW-
452 verging thrust system within the Jandaq metamorphic basement and ophiolites and possibly in the
453 Cretaceous cover, was followed by important dextral shearing along ENE-WSW and NE-SW strike-
454 slip faults associated to the formation of major transpressional structures and minor transtensional
455 faults suggesting a complex triclinic shearing. These structures of the second stage crosscut the
456 previously formed thrust sheets (Figure 8). The formation of thrust stacks with the same attitude
457 within the Cretaceous cover suggests a Cenozoic deformation age, as the deformed Upper Cretaceous
458 succession extends conformably at least to the Paleocene. More accurate time constraints on the age
459 of this deformation phase are provided by Javadi et al. (2013) and by Tadayon et al. (2019) along
460 other sectors of the GKDFS. Dextral faulting under a NW-SE compression follows in time thrust
461 stacking, and was active up to the middle Miocene (Javadi et al., 2013) or up to the Tortonian (Javadi
462 et al., 2015), from the age of the youngest rocks deformed by dextral faults along the western segment
463 of the GKDFS. Considering the thrust system displacing the upper Paleozoic Anarak Metamorphic
464 Complex related to the western termination of the right-lateral GKDFS, deformation could be
465 constrained to the latest Miocene (Javadi et al., 2015). Farbod et al. (2011) also proposed a NW-SE
466 compression on the basis of paleostress analyses along the central segment of the GKDFS given by
467 E-W dextral strike-slip faults measured in pre-Pliocene rocks, whereas recent Pliocene to Quaternary
468 faults are always consistent with a NE-SW contraction and a left-lateral shear sense of the fault.

469 Available data indicates that dextral shearing in response of a NW-SE directed shortening is not a
470 local feature strictly related to the GKDFS, but it is documented in other adjacent areas, like the
471 Alborz, during the late Cenozoic (Allen et al., 2003, Guest et al., 2006, Zanchi et al., 2006). The
472 Alborz orogenic belt acted as a distributed accommodation zone of dextral shearing up to the Kopeh
473 Dagh before oroclinal bending occurred (Mattei et al., 2017), as well as along secondary branches of
474 GKDFS (Nozaem et al., 2013).

475 A similar evolution of the regional stress regime is reported also in the Sistan belt of East Iran, with
476 a Miocene E-W compression followed by a CCW re-orientation to NE-SW and NNE-SSW
477 compressions during Pliocene and Quaternary, attesting full mechanical coupling of the Sistan Belt
478 with the Zagros region only after the Miocene (Jentzer et al., 2017).

479 This is a major critical point, as the studied area together with the Taknar (just NW of Kashmar,
480 Figure 1) and surrounding region display a NW-SE compression during the early Cenozoic, which is
481 at odds with the paleostress pattern reconstructed along the Zagros belt during pre-Pliocene times
482 through fault analyses (Navabpour et al., 2007). This suggests scarce coupling with the Zagros to the
483 west, whereas more similarities are evident with the whole region east of the Sanandaj-Sirjan.

484 We speculate that this particular stress and strain patterns can result from an independent stress field
485 induced by CCW rotations of rigid blocks between the closing Sistan Belt, subjected to an E-W
486 compression and active shortening in response to the deformation active along the Makran region
487 resulting from the motion of Arabia. On the other hand, Tadayon et al. (2019) find a good
488 correspondence in time among the main stages of the evolution of the Zagros belt, the Arabia-Eurasia
489 collision and the studied area of Central Iran.

490

491

492 **6.2 The remnants of the Paleotethys suture zone along the GKDFS and adjoining** 493 **areas**

494 The remnants of the Paleotethys suture zone have been recognized in several areas of Iran, from
495 Alborz, to NE Iran and Central Iran (Stocklin, 1974; Alavi, 1991; Ruttner et al., 1991; Ruttner 1993;
496 Zanchetta et al., 2013; Moghadam et al., 2015; Sheikholeslami et al., 2019; Sheikholeslami &
497 Koupeyma, 2012). In the Mashhad area of NE Iran the Paleotethys remnants consist of the
498 ultramafics-bearing Binalood metamorphic complex (Sheikholeslami et al., 2019; Sheikholeslami &
499 Khoupeyma, 2012), which have been related with a trench environment by Alavi (1991). Moving
500 NE-ward, the mid Paleozoic orogenic complexes of Darreh Anjir (Zanchetta et al., 2013; Moghadam
501 et al., 2015), the Permian turbiditic complex with carbonate olistoliths exposed between Mashhad
502 and Torbat Jam (Zanchetta et al., 2013), together with the Triassic volcanoclastic succession of
503 Aghdarband (Ruttner, 1991; Alavi et al., 1997; Balini et al., 2009; Zanchi et al., 2016; Balini et al.,
504 2019) point to the existence of an active convergent margin from the Devonian up to the Middle
505 Triassic. The Upper Triassic granitoids of Mashhad (Karimpour et al., 2010; Mirnejad et al., 2013)
506 and Torbat Jam (Zanchetta et al., 2013) intruded the deformed units providing a minimum age for
507 collision. The last significant tectonic event affecting the Paleotethys suture zone occurred during the
508 Early Jurassic (Sheikholeslami et al., 2019) with penetrative deformation and associated

509 metamorphism up to amphibolite facies conditions (Sheikholeslami et al., 2019; Sheikholeslami &
510 Khoupeyma, 2012).

511 Correlation among the described units of the Paleotethys suture of NE Iran and the dispersed crustal
512 fragments exposed in the NW border of the CEIM is a major conundrum of the crustal scale geology
513 of Iran. Systematic investigations of these blocks followed by regional scale correlations performed
514 in recent years (Bagheri & Stampfli, 2008; Zanchi et al., 2009b; Balini et al., 2009; Zanchi et al.,
515 2015; Berra et al., 2017; Zanchetta et al., 2018) suggest that the Paleotethys suture zone could have
516 been displaced along the GKDFS for several hundreds of kilometers.

517 The oldest units recognized close to Jandaq occur in the Godar-e-Siah Complex, where a Devonian
518 to Carboniferous succession described by Sharkowski et al. (1984) contains Carboniferous
519 brachiopod faunas and foraminifera with a northern European affinity (Berra et al., 2017). The U-Pb
520 zircon data obtained from granitoid boulders found in conglomerates exposed in the same area
521 provided a Late Devonian to Mississippian age (Berra et al., 2017), testifying to the occurrence of an
522 active magmatic arc during the Devonian and its subsequent deep erosion during the Paleozoic.

523 The occurrence of an active margin during the Carboniferous within the CEIM is provided by the
524 Carboniferous Anarak Metamorphic Complex (Bagheri & Stampfli, 2008; Zanchi et al., 2015), located
525 between Jandaq and the town of Anarak to the south, showing subduction-related HP-LT
526 metamorphism and deformation during the Late Carboniferous (Zanchi et al., 2015; Zanchetta et al.,
527 2018).

528 In addition, the Triassic volcanoclastic succession of Nakhlak (Figure 2), which contains deep-water
529 sediments interlayered with volcanic arc products, ammonite faunas, undeformed granitic clasts and
530 rock fragments derived from a metamorphic basement, has been correlated with the Aghdarband
531 succession (Ruttner, 1991; Alavi et al., 1997, Balini et al., 2009; Zanchi et al., 2009b; Balini et al.,
532 2019). The two areas are the only ones where a Lower to Middle Triassic deep water marine
533 succession deposited in an active arc environment crops out. During the same time, in fact, the entire
534 Iranian plate was covered by shallow sea carbonate platforms (Elika Fm.), pointing to a
535 paleogeographical affinity of the two successions currently separated by more than 600 kilometers.

536 The Posht-e-Badam Complex, located between the two dextral strike-slip Posht-e-Badam and
537 Chapedony faults, gives additional evidence of a displaced fragment of the Paleotethys suture within
538 the interior of the CEIM. Its present-day position has been interpreted as the result of large-scale
539 CCW of the Yazd Block along dextral large-scale sub-circular shear zones juxtaposing this unit
540 between the two Yazd and Tabas blocks (Bagheri & Stampfli, 2008). The Posht-e-Badam Complex
541 bears several similarities with the Anarak-Jandaq units (Davoudzadeh & Weber-Diefenbach, 1997),
542 as it shows Carboniferous metamorphic ages and it was intruded by Upper Triassic granites and

543 granodiorites (Ramezani & Tucker, 2003). Evidence of Cimmerian deformation and metamorphism
544 in this area was recently confirmed by ^{40}Ar - ^{39}Ar amphibole ages of ca. 220 Ma (Kargaranbafghi et
545 al., 2012).

546 Pirnia et al. (2020) also proposed possible displacements of large blocks related to the CCW rotations
547 of the CEIM, based on the strong similarities in composition and origin between the Sabzevar and
548 the Nain-Ashin ophiolites, now lying more than 300 km apart (Figure 1a). According to these authors,
549 both units derived from a suprasubduction volcanic arc setting, active during the Early Cretaceous
550 along the northern margin of the CEIM. This margin was possibly in continuity with the northern
551 portion of the Sistan Ocean and they were displaced, together with their continental basement, along
552 a dextral precursor of the GKDF during the Cenozoic. This new hypothesis is in contrast with
553 previous interpretations correlating Nain and Baft ophiolites to the same origin in a back-arc position
554 with respect to the Sanandaj-Sirjan Mesozoic active margin located to the SW of Central Iran (e.g.
555 Hassanzadeh & Wernicke, 2016).

556

557 **6.3 The CEIM blocks rotation and the GKDFS**

558 The idea of a strong internal rotation of continental blocks forming the CEIM was born forty years
559 ago (Davoudzadeh & Schmidt, 1981). It was supported by the first paleomagnetic data produced on
560 this area by Soffel et al. (1996), suggesting a CCW rotation along vertical axes of the entire region
561 up to 135° . Based on new paleomagnetic data, the total amount of these CCW rotations was evaluated
562 between 45° and 82° with an average of $66^\circ (\pm 13^\circ)$ in the Upper Jurassic of the Yazd, Tabas and Lut
563 blocks (Mattei et al., 2015). According to Mattei et al. (2012, 2015, 2017), the CEIM was affected by
564 two main stages of rotations (Figure 13). The former event caused an average rotation of about 30°
565 and occurred between the Late Jurassic and the Early Cretaceous (150 Ma to 100 Ma). This rotation
566 was related either with the northward propagation of the opening of the Sistan Ocean or with its
567 eastward subduction under the Afghan block. The occurrence of high-pressure rocks of Coniacian
568 age (Brocker et al., 2013) indicates that subduction was active during the Late Cretaceous. We
569 propose that the opening of the Sistan Ocean, rather than its closure, was a more probable cause for
570 the Early Cretaceous rotations (Jentzer et al., 2017). In addition, the occurrence of Albian radiolarites
571 and Albian-Aptian oceanic rocks in the Sistan region (Zarrinkoub et al., 2012) indicate an existing
572 oceanic environment.

573 Before rotations, the Yazd, Tabas and Lut blocks forming the CEIM were oriented WSW-ESE with
574 the Lut block facing southward the Neotethys, as proposed by Wilmsen et al. (2015). A subsequent
575 stage of paleomagnetic rotations occurred after the Oligocene producing a total CCW rotation of 35°
576 with 20° during the last 10 Myrs, following a long time lapse during which no rotations along vertical

577 axes were recorded within the CEIM. According to Mattei et al. (2012, 2015), Cenozoic rotations
578 accommodated NNE-SSW shortening related to the convergence between Arabia and Eurasia. In this
579 framework, N-S trending dextral faults favoured CCW rotations of the single blocks forming the
580 CEIM, whereas to the north of the Doruneh Fault, poor or no clockwise rotations occurred (Mattei et
581 al., 2012; Walker & Jackson, 2004). It is important to stress that these large-scale paleomagnetic
582 rotations are confined to the CEIM, as no such rotations were measured outside its borders, although
583 post-Miocene oroclinal bending is responsible for the present curvature of the Alborz Mountains to
584 the north, due to Arabia-Eurasia indentation in front of the rigid South Caspian Basin (Mattei et al.,
585 2015, 2017, 2019).

586 This two stages rotation model (Figure 13) can explain the scenario of differential displacement of
587 large crustal blocks within and around CEIM. The larger displacement shown by the upper Paleozoic
588 to Triassic Paleotethys fragments with respect to the horizontal separation occurring between the
589 Sabzevar and the Nain-Ashin arc-related “ophiolites” can be thus explained in terms of their different
590 age of formation. The Paleotethys suture was affected by the maximum amount of CCW vertical axes
591 rotations, which has been recorded at least from the Jurassic-Cretaceous boundary,
592 contemporaneously with the opening of the Sabzevar and Sistan oceanic basin around the CEIM.
593 Wrench tectonics accompanying the post-collisional stage of the Cimmerian orogeny (Zanchi et al.,
594 2016) may have favoured additional displacements starting from the end of the Triassic. The second
595 significant stage of CCW rotations occurred during the Cenozoic after a long time of null rotations
596 and can be directly related with the dextral activity of the Doruneh Fault System and related structures
597 as recognized by structural analyses carried out all along the fault zone. According to this idea, Javadi
598 et al. (2013) evaluated a Cenozoic displacement of about 280 kilometers along the GKDFS, which
599 can help to restore the Nain-Ashin ophiolites to their original position closer to Sabzevar and to
600 accomplish the entire rotations of the Paleotethys blocks up to the NW corner of the CEIM. The
601 approximate curvilinear geometry of the GKDFS and of the other major faults responsible for the
602 rotations of the Posht-e-Badam block are additional indications of the occurring rotation along a
603 stable pivot point which can be located in the southern part of the CEIM with limited variations
604 through time (Figure 13).

605 The CCW rotation of the CEIM crustal block could had been activated in response to the tectonic
606 evolution of adjacent areas to the east, i.e. the Makran subduction zone and the closure of the Sistan
607 Ocean, rather than to the progressive building of the Zagros belt. This interpretation is consistent with
608 the absence of rotation of the Sanandaj-Sirjan crustal block during the same time interval.

609

610 **7. Conclusions**

611 Integrated structural and stratigraphic analyses and detailed geological mapping of a ENE-WSW fault
612 system of regional importance (the Arusan Fault System) in the NE sector of the CEIM, just south of
613 the present-day active Great Kavir – Doruneh Fault, take to the following main results:

- 614 - The AFS, including two main fault strands (the western and eastern ones), shows dextral
615 motion all along its development, accompanied by transtensional and transpressional
616 structures. Based on crosscutting relationships, transpressional structures resulting in *en*
617 *échelon* folds and thrusts formed along the western segment during dextral shear. The eastern
618 segment shows relationships that are more complex, as thrust faults laterally pass to a dextral
619 transpressional shear zone which crosscut NW-SE normal faults and NNE-SSW left-lateral
620 strike-slip faults consistent with a dextral shear. Both segments of the AFS display similar
621 kinematic and geological features. Both fault zones juxtapose strongly uplifted Mesozoic
622 crystalline basement rocks including amphibolite facies metamorphic rocks and ophiolites to
623 the Cretaceous carbonate succession, which is underlain by the Chah Palang ?Upper Jurassic-
624 Lower Cretaceous conglomerates directly resting on the basement.
- 625 - Two main tectonic stages could be recognized in the Arusan area: (i) an older one related to
626 a NW-SE compression stacking the basement and the ophiolites in a NW-verging thrust fan;
627 (ii) a younger event related to the development of ENE-WSW dextral strike-slip faults that
628 crosscut and/or reactivate thrust faults related to the older event. Structures that could be
629 correlated with the first event, on the base of their trend and kinematics, also affect the
630 Cretaceous succession just south of Arusan, suggesting a post-Cretaceous, “mid” Cenozoic
631 deformation age.
- 632 - Paleostress analyses carried out in several sites along fault strike give homogeneous results,
633 with the main horizontal stress axes σ_1 and σ_3 trending respectively NW-SE and NE-SW in
634 a dominant transtensional regime.

635
636 The proposed structural reconstructions are consistent with the regional evolution recognized by
637 previous authors, pointing to dextral activity of the GKDFS up to the end of the Miocene, when the
638 fault zone flipped to left-lateral strike-slip motions.

639 Considering the continuity of the exposed portion of the AFS and its dimensions and related
640 structures, we propose that this fault may directly represent one of the main branches of the dextral
641 GKDFS, which was active before the Pliocene time interval. The GKDFS represents a well-
642 defined example of the large dextral shear zone bordering the northern boundary of the CEIM
643 during most of the Cenozoic connecting the central part of the fault, the Doruneh segment, with its
644 westernmost termination in the Ashin area.

645 Integrating our structural data with previous structural analyses on the GKDFS, available
646 paleomagnetic data and the updated information on the displaced fragments of the Paleotethyan and
647 Neotethyan ophiolites, we propose a simple geometrical model. The model restores these units to
648 their previous positions, in response to the CCW rotations occurred along vertical axes (Mattei et al.,
649 2015). The larger displacements shown by the Paleotethys units is explained by the larger rotations
650 occurring since the Triassic, with respect to the smaller displacements suffered by the Upper
651 Cretaceous Neotethyan ophiolites.

652 Several uncertainties on large block rotations and displacement of crustal blocks remain to be better
653 investigated, especially with concern to the evolution of the poorly known regions of the Sistan and
654 Makran orogens and to their role in the deformation of Central Iran.

655

656 **Acknowledgments**

657 We are deeply indebted with the Geological Survey of Iran of Teheran, for providing invaluable help
658 during fieldwork in Arusan. We are also grateful with the owner of the Potash Mine house, who
659 kindly hosted us during several weeks of work in the area.

660 The present project has been funded by the DARIUS PROGRAMME: “The Late Paleozoic to Eo-
661 Cimmerian Orogenic Complexes of Central Iran: a Still Unsolved Enigma” and by the PRIN2010-
662 2011 Italian MIUR project: “Birth and death of oceanic basins: geodynamic processes from rifting to
663 continental collision in Mediterranean and Circum-Mediterranean orogens”. It was carried out in the
664 frame of a Memorandum of Understanding between the Geological Survey of Iran and the
665 Department of Earth and Environmental Sciences of Milano-Bicocca University.

666

667 **References**

- 668 Alavi, M. (1991). Sedimentary and structural characteristics of the Paleo-Tethys remnants in
669 northeastern Iran. *Geological Society of America Bulletin*, 103(8), 983-992.
- 670 Alavi, M., Vaziri, H., Seyed Enami, K., & Lasemi, Y. (1997). The Triassic and associated rocks of
671 the Naxhlak and Aghdarband areas in central and northeastern Iran as remnants of the southern
672 Turanian active continental margin. *Geological Society of America Bulletin*, 109, 1563-1575.
- 673 Allen, M. B., Ghassemi, M. R., Shahrabi, M., & Qorashi, M. (2003). Accommodation of late
674 Cenozoic oblique shortening in the Alborz range, northern Iran. *Journal of Structural Geology*,
675 25(5), 659-672.
- 676 Angelier, J. (1984). Tectonic analysis of fault slip data sets. *Journal of Geophysical Research*, 89,
677 5835-5848.

- 678 Angelier, J. (1990). Inversion of field data in fault tectonics to obtain the regional stress-III. A new
679 rapid direct inversion method by analytical means. *Geophysical Journal International*, 103,
680 363-376.
- 681 Angelier, J. (2002). Inversion of earthquake focal mechanisms to obtain the seismotectonic stress
682 IV—a new method free of choice among nodal planes. *Geophysical Journal
683 International*, 150(3), 588-609.
- 684 Bagheri, S., & Stampfli, G. M. (2008). The Anarak, Jandaq and Posht-e-Badam metamorphic
685 complexes in central Iran: New geological data, relationships and tectonic implications.
686 *Tectonophysics*, 451, 123-155.
- 687 Bagheri, S., Madhanifard, R., & Zahabi, F. (2017). Kinematics of the Great Kavir fault inferred from
688 a structural analysis of the Pees Kuh Complex, Jandaq area, central Iran. *Tectonic Evolution,
689 Collision, and Seismicity of Southwest Asia: In Honor of Manuel Berberian's Forty-Five Years
690 of Research Contributions*, 525, 213-227.
- 691 Balini, M., Nicora, A., Berra F., Garzanti, F., Levera, M., Mattei M., et al. (2009). The Triassic
692 stratigraphic succession of Nakhlak (central Iran), a record from an active margin. In: M.F.
693 Brunet, M. Wilmsen, & J.W. Granath (Eds.), *South Caspian to Central Iran Basins* (Vol. 312,
694 pp. 287-321). Geological Society of London Special Publications.
- 695 Balini, M., Nicora, A., Zanchetta, S., Zanchi, A., Marchesi, R., Vuolo, I., et al. (2019). Olenekian to
696 Early Ladinian stratigraphy of the western part of the Aghdarband window (Kopeh-dag, NE
697 Iran). *Rivista Italiana di Paleontologia e Stratigrafia*, 125(1), 283-315.
- 698 Barrier, E., & Vrielynck, B. (2008). Palaeotectonic Maps of the Middle East, Atlas of 14 Maps.
699 CGMW/CCGM, Paris, France.
- 700 Berra, F., Zanchi, A., Angiolini, L., Vachard, D., Vezzoli, G., Zanchetta, S., et al. (2017). The upper
701 Palaeozoic Godar-e-Siah Complex of Jandaq: evidence and significance of a North
702 Palaeotethyan succession in Central Iran. *Journal of Asian Earth Sciences*, 138, 272-290.
- 703 Bröcker, M., Rad, G. F., Burgess, R., Theunissen, S., Paderin, I., Rodionov, N., & Salimi, Z. (2013).
704 New age constraints for the geodynamic evolution of the Sistan Suture Zone, eastern
705 Iran. *Lithos*, 170, 17-34.
- 706 Carey, E., & Brunier, B. (1974). Numerical-analysis of an elementary mechanical model applied to
707 study of a population of faults. *Comptes Rendus Hebdomadaires des Seances de l'Academie
708 des Sciences Serie D*, 279(11), 891-894.
- 709 Davoudzadeh, M., & Schmidt, K. (1981). Contribution to the paleogeography and stratigraphy of the
710 Upper Triassic to Middle Jurassic of Iran. *Neues Jahrbuch für Geologie und Paläontologie.
711 Abhandlungen*, 162(2), 137-163.

- 712 Davoudzadeh, M., & Weber-Diefenbach, K. (1997). Paleogeography, stratigraphy, and tectonics of
713 the tertiary of Iran. *Neues Jahrbuch für Geologie und Paläontologie-Abhandlungen*, 33-67.
- 714 Delvaux, D., & Sperner, B. (2003). Stress tensor inversion from fault kinematic indicators and focal
715 mechanism data: the TENSOR program. In: D. Nieuwland (Eds.), *New Insights into Structural*
716 *Interpretation and Modelling* (Vol. 212, pp. 75-100). Geological Society, London, Special
717 Publications.
- 718 Díaz-Azpiroz, M., Barcos, L., Balanyá, J. C., Fernández, C., Expósito, I., & Czeck, D. M. (2014).
719 Applying a general triclinic transpression model to highly partitioned brittle-ductile shear
720 zones: A case study from the Torcal de Antequera massif, external Betics, southern
721 Spain. *Journal of Structural Geology*, 68, 316-336.
- 722 Farbod, Y., Bellier, O., Shabanian, E., & Abbassi, M. R. (2011). Geomorphic and structural variations
723 along the Doruneh Fault System (central Iran). *Tectonics*, 30(6), TC6014,
724 doi:10.1029/2011TC002889.
- 725 Farbod, Y., Shabanian, E., Bellier, O., Abbassi, M. R., Braucher, R., Benedetti, L., et al. (2016).
726 Spatial variations in late Quaternary slip rates along the Doruneh Fault System (Central
727 Iran). *Tectonics*, 35(2), 386-406.
- 728 Fossen, H., & Cavalcante, G. C. G. (2017) Shear zones—a review. *Earth Science*
729 *Reviews*, 171, 434-455.
- 730 Fossen, H., & Tikoff, B. (1993). The deformation matrix for simultaneous pure shear, simple shear,
731 and volume change, and its application to transpression/transension tectonics. *Journal of*
732 *Structural Geology*, 15, 413-422.
- 733 Fossen, H., & Tikoff, B. (1998). Extended models of transpression and transtension, and application
734 to tectonic settings. In: R.E. Holdsworth, R.A. Strachan, & J.F. Dewey (Eds.), *Continental*
735 *Transpressional and Transtensional Tectonics* (Vol. 135, pp. 15-33). Geological Society,
736 London, Special Publications.
- 737 Fossen, H., Tikoff, B., & Teyssier, C. (1994). Strain modelling of transpressional and transtensional
738 deformation. *Norsk Geologisk Tidsskrift*, 74, 134-145.
- 739 Freund, R. (1970). Rotation of strike slip faults in Sistan, southeast Iran. *The Journal of*
740 *Geology*, 78(2), 188-200.
- 741 Guest, B., Axen, G. J., Lam, P. S., & Hassanzadeh, J. (2006). Late Cenozoic shortening in the west-
742 central Alborz Mountains, northern Iran, by combined conjugate strike-slip and thin-skinned
743 deformation. *Geosphere*, 2(1), 35-52.
- 744 Hassanzadeh, J., & Wernicke, B. P. (2016). The Neotethyan Sanandaj-Sirjan zone of Iran as an
745 archetype for passive margin-arc transitions. *Tectonics*, 35(3), 586-621.

- 746 Javadi, H. R., Esterabi Ashtiani, M., Guest, B., Yassaghi, A., Ghassemi, M. R., Shahpasandzadeh,
747 M., & Naeimi, A. (2015). Tectonic reversal of the western Doruneh Fault System: Implications
748 for Central Asian tectonics. *Tectonics*, *34*, 2034-2051.
- 749 Javadi, H. R., Ghassemi, M. R., Shahpasandzadeh, M., Guest, B., Ashtiani, M. E., Yassaghi, A., &
750 Kouhpeyma M. (2013). History of faulting on the Doruneh Fault System: implications for the
751 kinematic changes of the Central Iranian Microplate. *Geological Magazine*, *150*, 651-672.
- 752 Jentzer, M., Fournier, M., Agard, P., Omrani, J., Khatib, M. M., & Whitechurch, H. (2017). Neogene
753 to Present paleostress field in Eastern Iran (Sistan belt) and implications for regional
754 geodynamics. *Tectonics*, *36*(2), 321-339.
- 755 Jentzer, M., Whitechurch, H., Agard, P., Ulrich, M., Caron, B., Zarrinkoub, M. H., Kohansal, R.,
756 Miguet, L., Omrani, J., & Fournier, M. (2020). Late Cretaceous calc-alkaline and adakitic
757 magmatism in the Sistan suture zone (Eastern Iran): Implications for subduction polarity and
758 regional tectonics. *Journal of Asian Earth Sciences*, *204*, 104588.
- 759 Kargaranbafghi, F., Neubauer, F., & Genser, J. (2011). Cenozoic kinematic evolution of southwestern
760 Central Iran: Strain partitioning and accommodation of Arabia–Eurasia convergence.
761 *Tectonophysics*, *502*(1-2), 221-243.
- 762 Kargaranbafghi, F., Neubauer, F., Genser, J., Faghih, A., & Kusky, T. (2012). Mesozoic to Eocene
763 ductile deformation of western Central Iran: From Cimmerian collisional orogeny to Eocene
764 exhumation. *Tectonophysics*, *564*, 83-100.
- 765 Karimpour, M. H., Farmer, G. L., & Stern, C. R. (2010). Geochronology, radiogenic isotope
766 geochemistry, and petrogenesis of Sangbast Paleo-Tethys monzogranite, Mashhad, Iran.
767 *Iranian Journal of Crystallography and Mineralogy*, *17*(4), 703-715.
- 768 Kent, D. V., & Muttoni, G. (2020). Pangea B and the Late Paleozoic Ice Age. *Palaeogeography*,
769 *Palaeoclimatology*, *Palaeoecology*, 109753, <https://doi.org/10.1016/j.palaeo.2020.109753>.
- 770 Mattei, M., Cifelli, F., Alimohammadian, H., Rashid, H., Winkler, A., & Sagnotti, L. (2017).
771 Oroclinal bending in the Alborz Mountains (Northern Iran): New constraints on the age of
772 South Caspian subduction and extrusion tectonics. *Gondwana Research*, *42*, 13-28.
- 773 Mattei, M., Cifelli, F., Muttoni, G., & Rashid, H. (2015). Post-Cimmerian (Jurassic-Cenozoic)
774 paleogeography and vertical axis tectonic rotations of Central Iran and the Alborz Mountains.
775 *Journal of Asian Earth Sciences*, *102*, 92-101.
- 776 Mattei, M., Cifelli, F., Muttoni, G., Zanchi, A., Berra, F., Mossavvari, F., & Eshraghi, S. A. (2012).
777 Neogene block-rotation in Central Iran: evidence from paleomagnetic data. *Geological Society*
778 *of America Bulletin*, *124*, 943-956.

- 779 Mattei, M., Visconti, A. L., Cifelli, F., Nozaem, R., Winkler, A., & Sagnotti, L. (2019). Clockwise
780 paleomagnetic rotations in northeastern Iran: Major implications on recent geodynamic
781 evolution of outer sectors of the Arabia-Eurasia collision zone. *Gondwana Research*, *71*, 194-
782 209.
- 783 Means, W. D., Hobbs, B. E., Lister, B. E., & Williams, P. F. (1980). Vorticity and non-coaxiality
784 in progressive deformations. *Journal of Structural Geology*, *2*, 371-378.
- 785 Mirnejad, H., Lalonde, A. E., Obeid, M., & Hassanzadeh, J. (2013). Geochemistry and petrogenesis
786 of Mashhad granitoids: An insight into the geodynamic history of the Paleo-Tethys in northeast
787 of Iran. *Lithos*, *170*, 105-116.
- 788 Moghadam, H. S., Khademi, M., Hu, Z., Stern, R. J., Santos, J. F., & Wu, Y. (2015). Cadomian
789 (Ediacaran–Cambrian) arc magmatism in the ChahJam–Biarjmand metamorphic complex
790 (Iran): Magmatism along the northern active margin of Gondwana. *Gondwana Research*, *27*(1),
791 439-452.
- 792 Molnar, P., & Tapponnier, P. (1975). Cenozoic tectonics of Asia: effects of a continental collision.
793 *Science*, *189*(4201), 419-426.
- 794 Morin, J., Jolivet, M., Robin, C., Heilbronn, G., Barrier, L., Bourquin, S., & Jia, Y. (2018). Jurassic
795 paleogeography of the Tian Shan: An evolution driven by far-field tectonics and climate. *Earth-
796 Science Reviews*, *187*, 286-313.
- 797 Mount, V. S. & Suppe, J. (1987). State of stress near the San Andreas fault: Implications for wrench
798 tectonics. *Geology*, *15*(12), 1143-1146.
- 799 Muttoni, M., Mattei, M., Balini, M., Zanchi, A., Gaetani, M., & Berra, F. (2009). The drift history of
800 Iran from the Ordovician to the Triassic. In: M.F. Brunet, M. Wilmsen, & J.W. Granath (Eds.),
801 *South Caspian to Central Iran Basins* (Vol. 312, pp. 7-29). Geological Society of London
802 Special Publications.
- 803 Navabpour, P., Angelier, J., & Barrier, E. (2007). Cenozoic post-collisional brittle tectonic history
804 and stress reorientation in the High Zagros Belt (Iran, Fars Province). *Tectonophysics*, *432*(1-
805 4), 101-131.
- 806 Nozaem, R., Mohajjel, M., Rossetti, F., Della Seta, M., Vignaroli, G., Yassaghi, A., Salvini, F., and
807 Eliassi, M., 2013, Post-Neogene right-lateral strike-slip tectonics at the north-western edge of
808 the Lut block (Kuh-eSarhangi fault), central Iran. *Tectonophysics*, *589*, 220–233.
- 809 Omrani, H., Moazzen, M., Oberhänsli, R., Altenberger, U., & Lange, M. (2013). The Sabzevar
810 blueschists of the North-Central Iranian micro-continent as remnants of the Neotethys-related
811 oceanic crust subduction. *International Journal of Earth Sciences*, *102*(5), 1491-1512.

812 Onderdonk, N. W. (2005). Structures that accommodated differential vertical axis rotation of the
813 western Transverse Ranges, California. *Tectonics*, 24(4), TC4018.

814 Petit, J.-P., & Barquins, M. (1988). Can natural faults propagate under Mode II
815 conditions?, *Tectonics*, 7(6), 1243-1256, doi:10.1029/TC007i006p01243

816 Pirnia, T., Saccani, E., Torabi, G., Chiari, M., Goričan, Š., & Barbero, E. (2020). Cretaceous tectonic
817 evolution of the Neo-Tethys in Central Iran: Evidence from petrology and age of the Nain-
818 Ashin ophiolitic basalts. *Geoscience Frontiers*, 11(1), 57-81.

819 Ramezani, J., & Tucker, R. D. (2003). The Saghand region, central Iran: U-Pb geochronology,
820 petrogenesis and implications for Gondwana tectonics. *American Journal of Science*, 303(7),
821 622-665.

822 Romanko, E., (1969). Mesr 6957 and Arusan 7059 sheets of the Geological Map of Iran at 1: 100,000
823 scale.

824 Ron, H., Freund, R., Garfunkel, Z., & Nur, A. (1984). Block rotation by strike-slip faulting: Structural
825 and paleomagnetic evidence. *Journal of Geophysical Research: Solid Earth*, 89(B7), 6256-
826 6270.

827 Rossetti, F., Nozaem, R., Lucci, F., Vignaroli, G., Gerdes, A., Nasrabadi, M., & Theye, T. (2015).
828 Tectonic setting and geochronology of the Cadomian (Ediacaran-Cambrian) magmatism in
829 central Iran, Kuh-e-Sarhangi region (NW Lut Block). *Journal of Asian Earth Sciences*, 102, 24-
830 44.

831 Ruttner, A. W. (1993). Southern borderland of Triassic Laurasia in north-east Iran. *Geologische*
832 *Rundschau*, 82(1), 110-120.

833 Ruttner, A. W., Brandner, R., & Kirchner, E. (1991). Geology of the Aghdarband area (kopet Dagh,
834 NE-Iran). *Abhandlungen der Geologischen Bundesanstalt*, 38, 7-79.

835 Shabanian, E., Bellier, O., Siame, L., Arnaud, N., Abbassi, M. R., & Cochemé, J.-J. (2009). New
836 tectonic configuration in NE Iran: active strike-slip faulting between the Kopeh Dagh and
837 Binalud mountains. *Tectonics*, 28(5), TC5002, doi: 10.1029/2008TC002444.

838 Sharkovski, M., Susov, M., & Krivyakin, B. (1984). Geology of the Anarak area (central Iran).
839 Explanatory text of the Anarak quadrangle map 1:250.000. Geological Survey of Iran, V/O
840 "Technoexport" USSR Ministry of Geology, Reports, TE/No. 19, 143 pp. Moscow.

841 Sheikholeslami, M. R., & Kouhpeyma, M. (2012). Structural analysis and tectonic evolution of the
842 eastern Binalud Mountains, NE Iran. *Journal of Geodynamics*, 61, 23-46.

843 Sheikholeslami, M. R., Oberhänsli, R., & Ghassemi, M. R. (2019). Transpression tectonics in the
844 eastern Binalud Mountains, northeast Iran; Insight from finite strain analysis, vorticity and
845 $^{40}\text{Ar}/^{39}\text{Ar}$ dating. *Journal of Asian Earth Sciences*, 179, 219-237.

846 Shirdashtzadeh, N., Torabi, G., & Schaefer, B. (2018). A magmatic record of Neoproterozoic to
847 Paleozoic convergence between Gondwana and Laurasia in the northwest margin of the
848 Central-East Iranian Microcontinent. *Journal of Asian Earth Sciences*, *166*, 35-47.

849 Soffel, H. C., Schmidt, S., Davoudzadeh, M., & Rolf, C. (1996). New palaeomagnetic data from
850 Central Iran and a Triassic palaeoreconstruction. *Geologische Rundschau*, *85*(2), 293-302.

851 Sonder, L. J., Jones, C. H., Salyards, S. L., & Murphy, K. M. (1994). Vertical axis rotations in the
852 Las Vegas Valley Shear Zone, southern Nevada: Paleomagnetic constraints on kinematics and
853 dynamics of block rotations. *Tectonics*, *13*(4), 769-788.

854 Stöcklin, J. (1974). Possible ancient continental margins in Iran. In *The geology of continental*
855 *margins* (pp. 873-887). Springer, Berlin, Heidelberg.

856 Storetvedt, K. M. (1974). A possible large-scale sinistral displacement along the Great Glen Fault in
857 Scotland. *Geological Magazine*, *111*(1), 23-30.

858 Storetvedt, K. M. (1987). Major late Caledonian and Hercynian shear movements on the Great Glen
859 Fault. *Tectonophysics*, *143*(4), 253-267.

860 Storti, F., Holdsworth, R. E., & Salvini, F. (2003). Intraplate strike-slip deformation belts. *Geological*
861 *Society, London, Special Publications*, *210*(1), 1-14.

862 Tadayon, M., Rossetti, F., Zattin, M., Calzolari, G., Nozaem, R., Salvini, F., et al. (2019). The long-
863 term evolution of the Doruneh Fault region (Central Iran): A key to understanding the spatio-
864 temporal tectonic evolution in the hinterland of the Zagros convergence zone. *Geological*
865 *Journal*, *54*(3), 1454-1479.

866 Tadayon, M., Rossetti, F., Zattin, M., Nozaem, R., Calzolari, G., Madanipour, S., & Salvini, F.
867 (2017). The post-eocene evolution of the Doruneh Fault region (central Iran): The intraplate
868 response to the Reorganization of the Arabia-Eurasia collision zone. *Tectonics*, *36*(12), 3038-
869 3064.

870 Tapponnier, P., Lacassin, R., Leloup, P. H., Schärer, U., Dalai, Z., Haiwei, W., Xiaohan, L.,
871 Shaocheng, J., Lianshang, Z., & Jiayou, Z. (1990). The Ailao Shan/Red River metamorphic
872 belt: tertiary left-lateral shear between Indochina and South China. *Nature*, *343*(6257), 431-
873 437.

874 Torabi, G. (2009). Chromitite potential in mantle peridotites of the Jandaq ophiolite (central
875 Iran). *Comptes Rendus Geoscience*, *341*(12), 982-992.

876 Torabi, G. (2012). Late Permian post-ophiolitic trondhjemites from Central Iran: a mark of
877 subduction role in growth of Paleozoic continental crust. *Island Arc*, *21*(3), 215-229.

878 Truesdell, C. (1953). Two measures of vorticity. *Journal of Rational Mechanics and Analysis*,
879 *2*, 173-217.

- 880 Walker, R., & Jackson, J. (2004). Active tectonics and late Cenozoic strain distribution in central and
881 eastern Iran. *Tectonics*, 23(5), TC5010.
- 882 Weijermars, R. (1991). The role of stress in ductile deformation. *Journal of Structural Geology*, 13,
883 1061-1078.
- 884 Wilmsen, M., Berensmeier, M., Fürsich, F. T., Majidifard, M. R., & Schlagintweit, F. (2018). A Late
885 Cretaceous epeiric carbonate platform: the Haftoman Formation of central Iran. *Facies*, 64(2),
886 1-24.
- 887 Wilmsen, M., Berensmeier, M., Fürsich, F. T., Schlagintweit, F., Hairapetian, V., Pashazadeh, B., &
888 Majidifard, M. R. (2020). Mid-Cretaceous biostratigraphy (ammonites, inoceramid bivalves
889 and foraminifers) at the eastern margin of the Anarak Metamorphic Complex (Central Iran).
890 *Cretaceous Research*, 110, 104411.
- 891 Wilmsen, M., Fürsich, F. T., & Majidifard, M. R. (2015). An overview of the Cretaceous stratigraphy
892 and facies development of the Yazd Block, western Central Iran. *Journal of Asian Earth
893 Sciences*, 102, 73-91.
- 894 Zanchetta, S., Berra, F., Zanchi, A., Bergomi, M., Caridroit, M., Nicora, M., & Heidarzadeh, G.
895 (2013). The record of the Late Palaeozoic active margin of the Palaeotethys in NE Iran:
896 Constraints on the Cimmerian orogeny. *Gondwana Research*, 24, 1237-1266.
- 897 Zanchetta, S., Malaspina, N., Zanchi, A., Benciolini, L., Martin, S., Javadi, H. R., & Kouhpeyma, M.
898 (2018). Contrasting subduction–exhumation paths in the blueschists of the Anarak
899 Metamorphic Complex (Central Iran). *Geological Magazine*, 155(2), 316-334.
900 doi:10.1017/S0016756817000218
- 901 Zanchi, A., Berra, F., Mattei, M., Ghassemi, M. R., & Sabouri, J. (2006). Inversion tectonics in central
902 Alborz, Iran. *Journal of Structural Geology*, 28(11), 2023-2037.
- 903 Zanchi, A., Malaspina, N., Zanchetta, S., Berra, F., Benciolini, L., Bergomi, M., et al. (2015). The
904 Cimmerian accretionary wedge of Anarak, Central Iran. *Journal of Asian Earth Sciences*, 102,
905 45-72.
- 906 Zanchi, A., Zanchetta, S., Balini, M., & Ghassemi, M. R. (2016). Oblique convergence during the
907 Cimmerian collision: Evidence from the Triassic Aghdarband Basin, NE Iran. *Gondwana
908 Research*, 38, 149-170
- 909 Zanchi, A., Zanchetta, S., Berra, F., Mattei, M., Garzanti, E., Molyneux, S., et al. (2009a). The Eo-
910 Cimmerian (Late? Triassic) orogeny in north Iran. In: M.F. Brunet, M. Wilmsen, & J.W.
911 Granath (Eds.), *South Caspian to Central Iran Basins* (Vol. 312, pp. 31-55). Geological Society
912 of London Special Publications.

913 Zanchi, A., Zanchetta, S., Garzanti, E., Balini, M., Berra, F., Mattei, M., & Muttoni, G. (2009b). The
914 Cimmerian evolution of the Nakhlak-Anarak area, central Iran, and its bearing for the
915 reconstruction of the history of the Eurasian margin. In: M.F. Brunet, M. Wilmsen, & J.W.
916 Granath (Eds.), *South Caspian to Central Iran Basins* (Vol. 312, pp. 261-286). Geological
917 Society of London Special Publications.

918 Zarrinkoub, M. H., Pang, K. N., Chung, S. L., Khatib, M. M., Mohammadi, S. S., Chiu, H. Y., & Lee,
919 H. Y. (2012). Zircon U–Pb age and geochemical constraints on the origin of the Birjand
920 ophiolite, Sistan suture zone, eastern Iran. *Lithos*, *154*, 392-405.

921 Zoback, M. L. (1992). First-and second-order patterns of stress in the lithosphere: The World Stress
922 Map Project. *Journal of Geophysical Research: Solid Earth*, *97*(B8), 11703-11728.

923

924

925

926

927

928

929

930

931

932

933

934

935

936

937

938

939

940

941

942

943

944 **Table**

| Site | | Data | Used | σ_1 | | | σ_2 | | | σ_3 | | | Ratio R | Ratio R' | | ANG | | F5 | st-dev | QRrwsn | QRt | LAT. | LONG. |
|-----------------------------------|---------------|------|------|------------|--------|------------|------------|--------|------------|------------|--------|------------|---------|----------|----|-------|-------|-------|--------|----------|----------|-------------|-------------|
| | | | | trend | plunge | 1 σ | trend | plunge | 1 σ | trend | plunge | 1 σ | | | | | | | | | | | |
| <i>NW-verging thrust stacking</i> | | | | | | | | | | | | | | | | | | | | | | | |
| I13-12 | AR-OPH | 19 | 16 | 142 | 15 | 12.4 | 51 | 6 | 9.3 | 301 | 74 | 9.8 | 0.31 | 2.31 | | 12.50 | 6.80 | 6.60 | 6.60 | C | C | 34° 05' 54" | 55° 01' 49" |
| <i>NE-SW dextral shearing</i> | | | | | | | | | | | | | | | | | | | | | | | |
| I15-15 | AWF | 4 | 4 | 98 | 79 | 19.9 | 318 | 8 | 27.7 | 227 | 7 | 23.4 | 0.33 | 0.33 | E | 9.00 | 5.40 | 3.30 | 2.20 | E | E | 34° 07' 02" | 55° 02' 46" |
| I15-16/17 | AWF | 7 | 6 | 109 | 2 | 26.4 | 356 | 73 | 26.8 | 201 | 15 | 12.5 | 0.92 | 1.08 | TT | 3.80 | 2.50 | 2.20 | 3.10 | D | D | 34° 07' 01" | 55° 03' 10" |
| I15-11/12 | AWF | 10 | 8 | 126 | 20 | 13.1 | 335 | 68 | 16.4 | 219 | 10 | 13.1 | 0.1 | 1.9 | TP | 7.10 | 7.20 | 2.60 | 4.10 | D | D | 34° 07' 17" | 55° 04' 8" |
| I15-9/37 | AWF | 7 | 6 | 97 | 31 | 12.2 | 255 | 57 | 10.5 | 1 | 10 | 6.7 | 0.48 | 1.52 | SS | 10.70 | 5.30 | 4.80 | 2.50 | D | D | 34° 07' 29" | 55° 04' 40" |
| I15-32 | MA | 4 | 4 | 137 | 1 | 18.9 | 46 | 67 | 29.5 | 227 | 23 | 28.3 | 0.37 | 1.63 | SS | 7.90 | 8.30 | 4.40 | 4.40 | E | E | 34° 09' 05" | 55° 11' 04" |
| I14-6 | AEF | 4 | 4 | 101 | 22 | 20.2 | 311 | 65 | 32.7 | 196 | 11 | 34.8 | 0.19 | 1.81 | TP | 9.10 | 5.80 | 4.90 | 2.30 | E | E | 34° 06' 04" | 55° 00' 08" |
| I15-1/21 | AEF | 10 | 10 | 310 | 17 | 8.6 | 73 | 61 | 18.8 | 212 | 23 | 19.7 | 0.3 | 1.7 | TP | 13.80 | 10.70 | 13.00 | 8.60 | C | C | 34° 07' 22" | 55° 05' 24" |
| I15-2/22 | AEF | 7 | 6 | 288 | 11 | 30.2 | 133 | 78 | 30.1 | 19 | 5 | 8.7 | 0.86 | 1.14 | TT | 11.70 | 10.00 | 10.00 | 8.20 | D | D | 34° 07' 10" | 55° 04' 58" |
| I15-23/24/25 | AEF | 11 | 8 | 297 | 19 | 49.1 | 93 | 70 | 53 | 205 | 8 | 12.4 | 0.96 | 1.04 | TT | 9.00 | 9.50 | 6.80 | 6.60 | D | D | 34° 07' 04" | 55° 04' 55" |
| I17-1 | AEF | 11 | 8 | 303 | 18 | 18.9 | 159 | 68 | 27.1 | 37 | 12 | 24.7 | 0.2 | 1.8 | TP | 9.10 | 8.60 | 4.50 | 6.80 | D | D | 34° 06' 56" | 55° 04' 34" |
| I14-22 | AEF | 21 | 16 | 277 | 10 | 12.1 | 125 | 79 | 22.3 | 8 | 5 | 20.7 | 0.42 | 1.58 | SS | 10.50 | 8.40 | 7.80 | 7.40 | B | B | 34° 05' 36" | 55° 02' 35" |
| I17-5/6 | AEF | 10 | 9 | 305 | 12 | 3.4 | 130 | 78 | 14.1 | 35 | 1 | 14.4 | 0.8 | 1.2 | TT | 7.50 | 7.30 | 8.20 | 7.00 | D | D | 34° 04' 38" | 55° 01' 30" |
| I15-4 | NSF | 18 | 15 | 93 | 14 | 9.5 | 184 | 3 | 13 | 284 | 75 | 10.9 | 0.18 | 2.18 | TP | 13.20 | 8.90 | 7.10 | 5.60 | C | C | 34° 03' 43" | 55° 01' 38" |

945

946

947

948

949

950

951

952 **Table 1.** Relevant information from stress inversion with Wintensor software (Delvaux & Sperner,
953 2003). Location of analysed sites in previous figures. AR-OPH: Arusan Ophiolites AWF: Arusan
954 Western Fault; AEF: Arusan Eastern Fault; MA: Mohammad Abad. Data: total number of
955 measurements; Used: number of accepted faults for stress inversion; trend/plunge of the main stress
956 axes σ_1 , σ_2 , and σ_3 with $\sigma_1 \geq \sigma_2 \geq \sigma_3$, with 1 sigma standard deviation; stress ratio R $(\sigma_2 - \sigma_3) / (\sigma_1 - \sigma_3)$;
957 tectonic stress regime index R' and its 1 sigma standard deviation (StDev). $R' = R$ when σ_1 is vertical
958 (extensional stress regime), $R' = 2 - R$ when σ_2 is vertical (strike-slip stress regime), $R' = 2 + R$ when
959 σ_3 is vertical (compressional stress regime). Quality estimator R_{wsm} takes into account the number
960 of faults measurements accepted on the total number of the faults used for the inversion and the
961 accuracy of the evaluation of the slip sense (World Stress Map project, Zoback, 1992). Quality
962 estimator R_t also considers the heterogeneity of the fault data orientations (Delvaux & Sperner, 2003);
963 both indexes range from A (best quality) to E (worst quality). Solutions were accepted for values of
964 the F5 misfit function < 30 (range 0-360 from perfect fit to complete misfit) and single values of the
965 angle $\alpha < 30^\circ$ between the slip vector on the fault plane and the computed shear stress. F5 is an
966 iterative function minimising the angle α , as well as the normal and shear stresses magnitudes
967 favouring the slip on the plane.

968

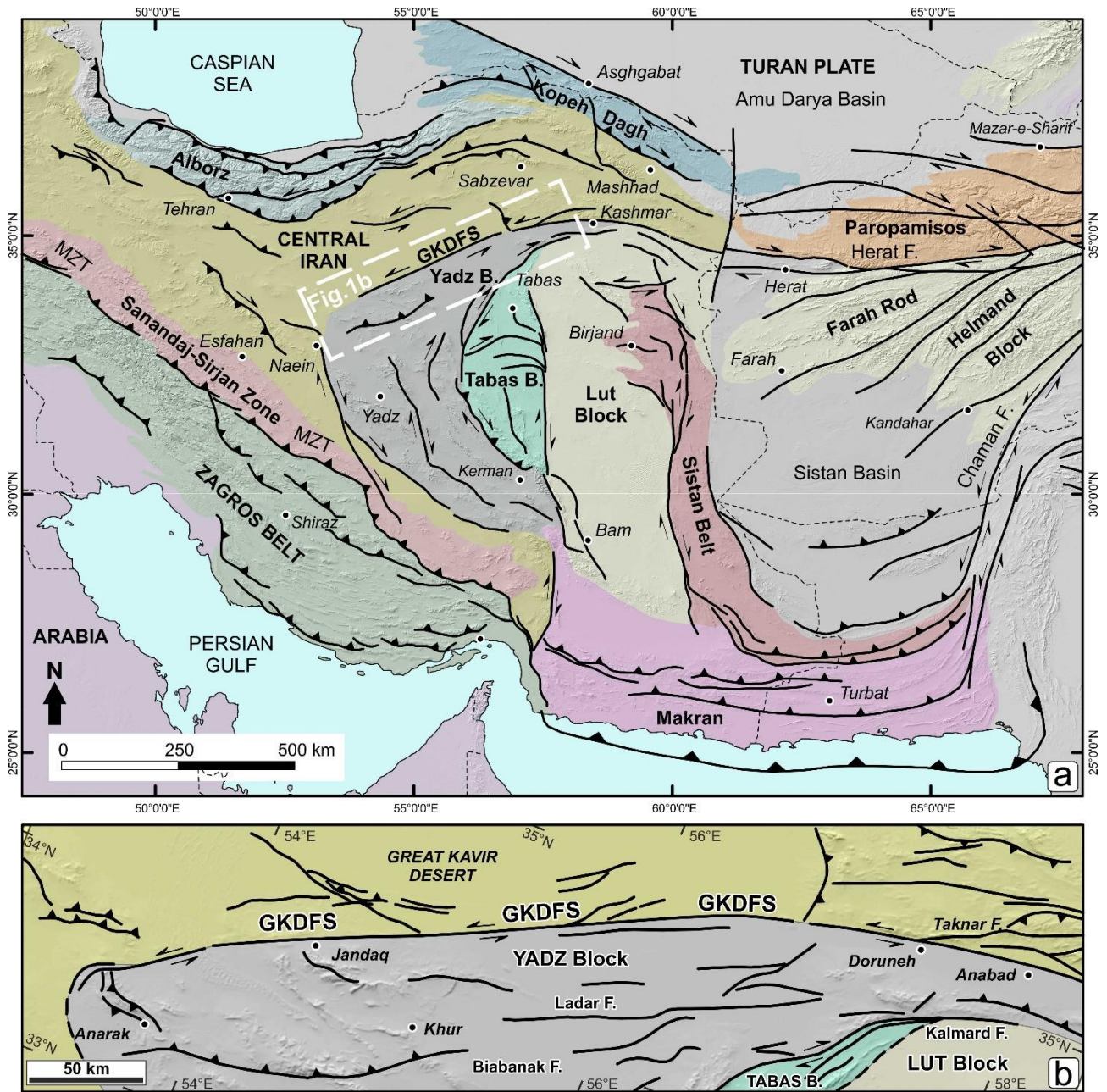
969

970

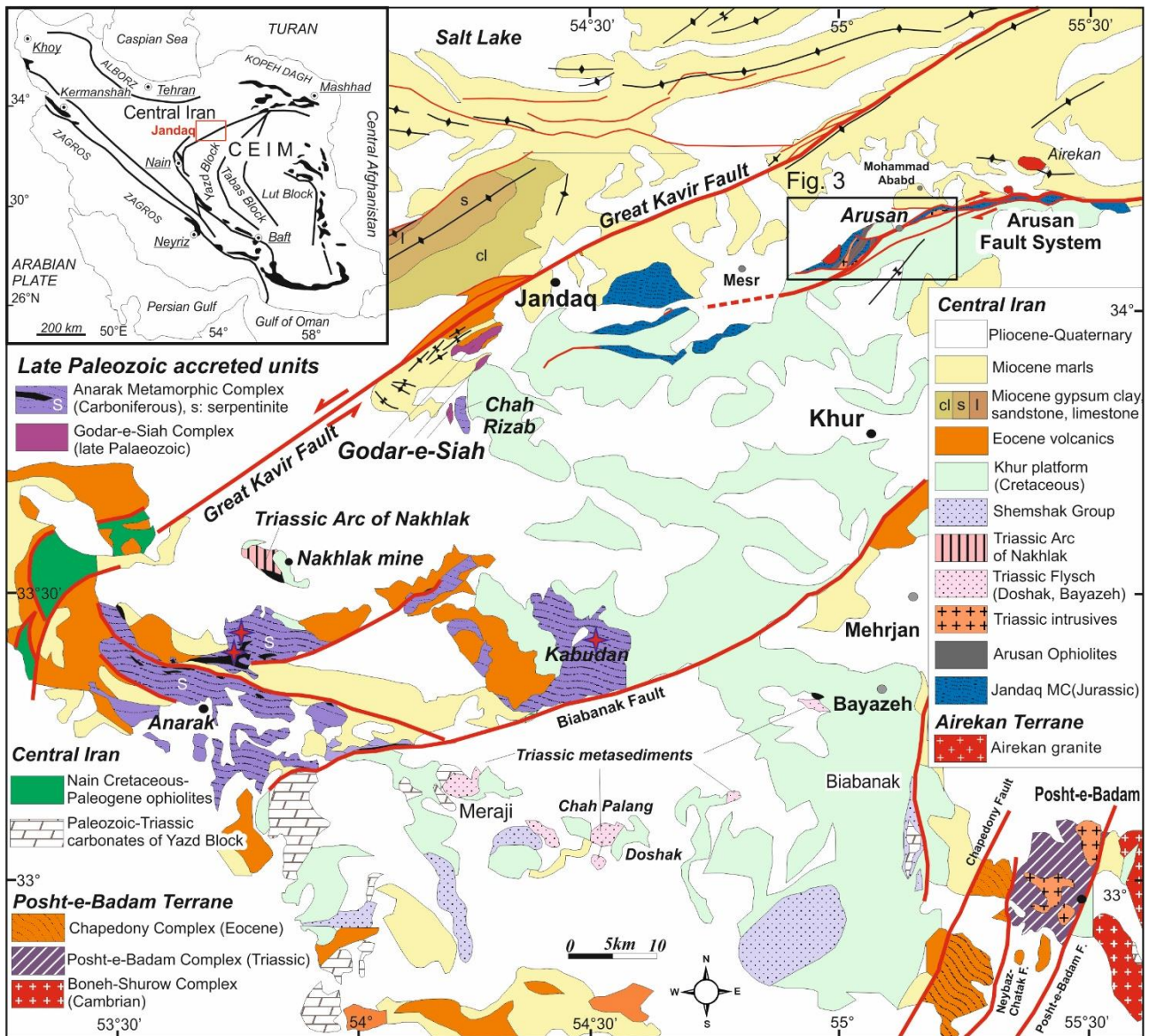
971

972

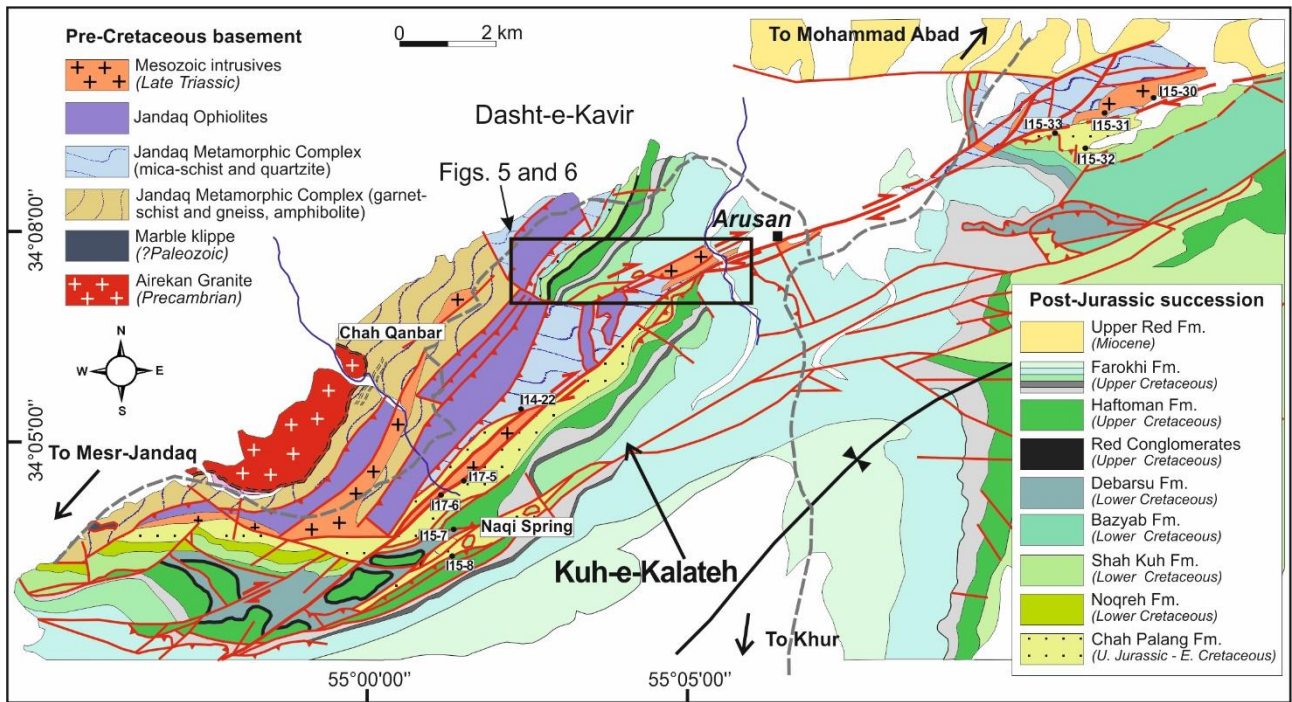
973



977 **Figure 1.** (a) General of Iran and surrounding areas extending to Afghanistan with the main fault
 978 zones. (b) Simplified structural map of the Great Kavir Doruneh Fault System (GKDFS), location in
 979 Figure 1a; modified from Javadi et al., 2013.

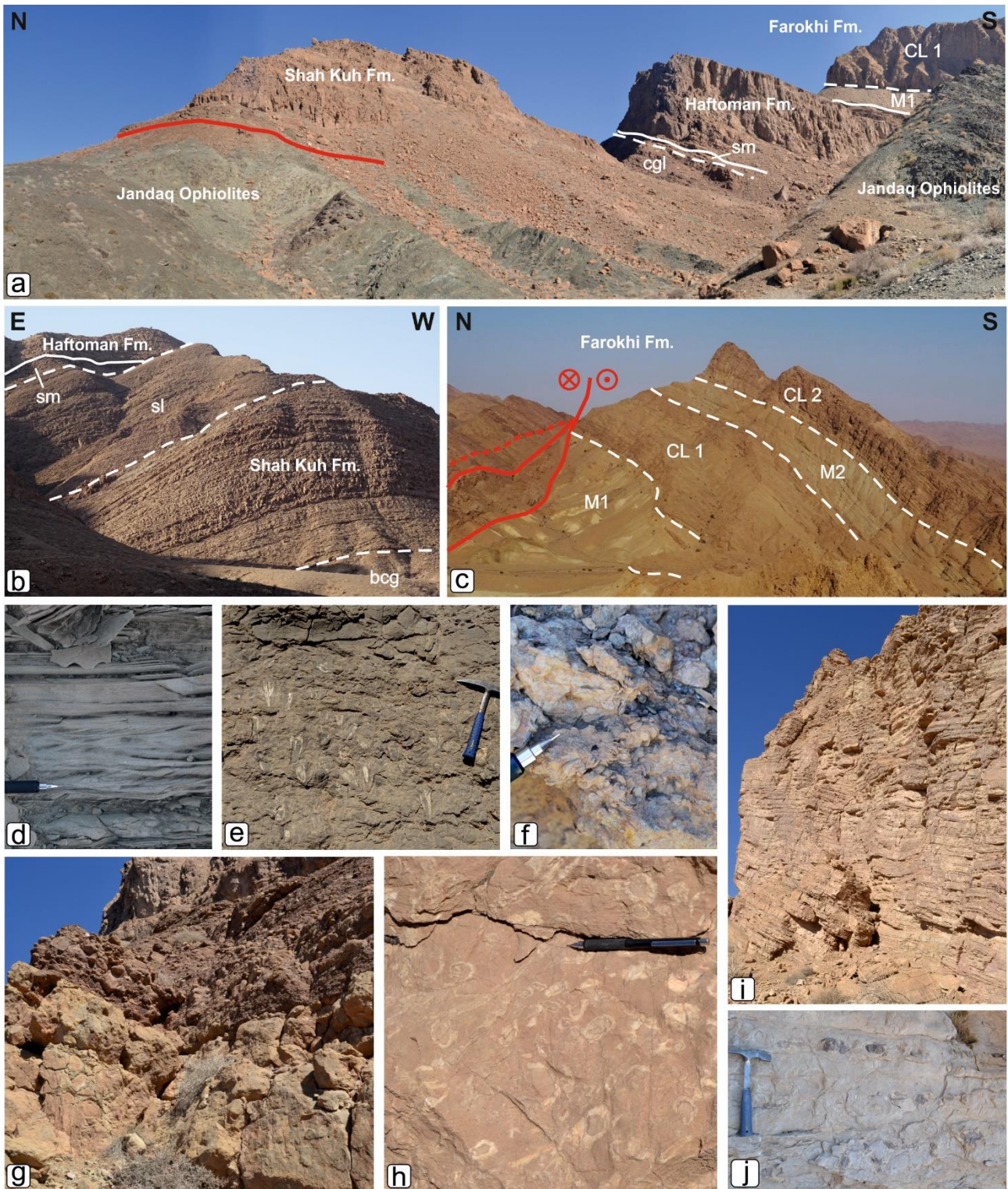


980
 981 **Figure 2.** Simplified structural map of the NW corner of Central Iran, with location of Figure 3;
 982 modified from Bagheri & Stampfli (2008) and from Berra et al. (2017), according to our original
 983 information. CEIM: Central Eastern Iran Microplate.



984

985 **Figure 3.** Geologic map of the Arusan area, modified from the Arusan and Mesr sheets of the
 986 Geological map of Iran (1:100,000; Romanko et al., 1979) according to our field survey. The location
 987 of some structural sites not present in the following maps are reported. The square shows the position
 988 of Figures 5 and 6.



989
 990 **Figure 4.** The Cretaceous succession exposed north of Kuhr close to Arusan. (a) View of the
 991 Cretaceous succession non-conformably covering the metamorphic basement close to cross section
 992 E-E' (Figure 7): a thick conglomerate unit (referred to as Haftoman Fm. by Wilmsen et al. 2015) is
 993 present between the Shah Kuh Formation and the limestone of the Haftoman Formation. (b) View of
 994 the succession on the north-western side of the study area, where the conglomeratic unit (Figure 4a)
 995 is not present. (c) The Farokhi Formation, south of a major branch of the AFS close to the Naqi Spring
 996 (Figure 3); note the alternation of marly and calcareous units. (d) Current ripples in quartz-rich

997 sandstone of the Chah Palang Formation. E: rudists in life position in the Shah Kuh Formation. (f)
998 Bioclastic silty rudstone with Orbitolinid macroforaminifera in the upper part of the Shah Kuh
999 Formation. (g) Erosional surface between the massive limestone of the Shah Kuh Formation and the
1000 overlying, poorly selected conglomerates with carbonate clasts. (h) Typical aspect of the rudist
1001 limestone of the Haftoman Formation. (i) Bedded fine-grained packstone with chert of the lower
1002 cherty limestone marking the drowning recorded by the Haftoman Formation. (j) Close-up view of
1003 chert nodules in fine-grained pelagic mudstone/wackestone of the upper cherty limestone.
1004 bcg: conglomerate at the base of the Shah Kuh Formation; sl: silty limestone, sm: silty marl (at the
1005 base of the Haftoman Fm.); cgl: red conglomerate (Haftoman Fm. sensu Wilmsen et al., 2015); M1:
1006 lower marls; CL1: lower cherty limestone; M2: upper marls; CL2: upper cherty limestone.

1007

1008

1009

1010

1011

1012

1013

1014

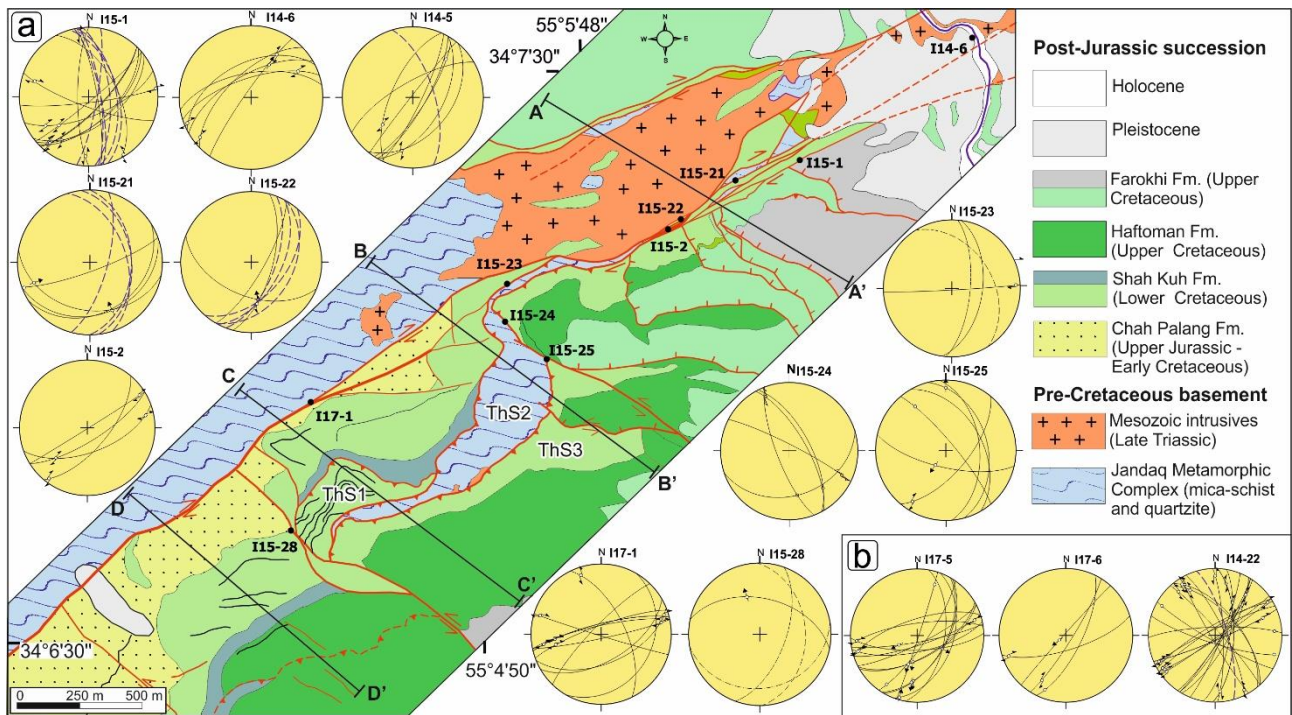
1015

1016

1017

1018

1019



1020

1021

1022

1023

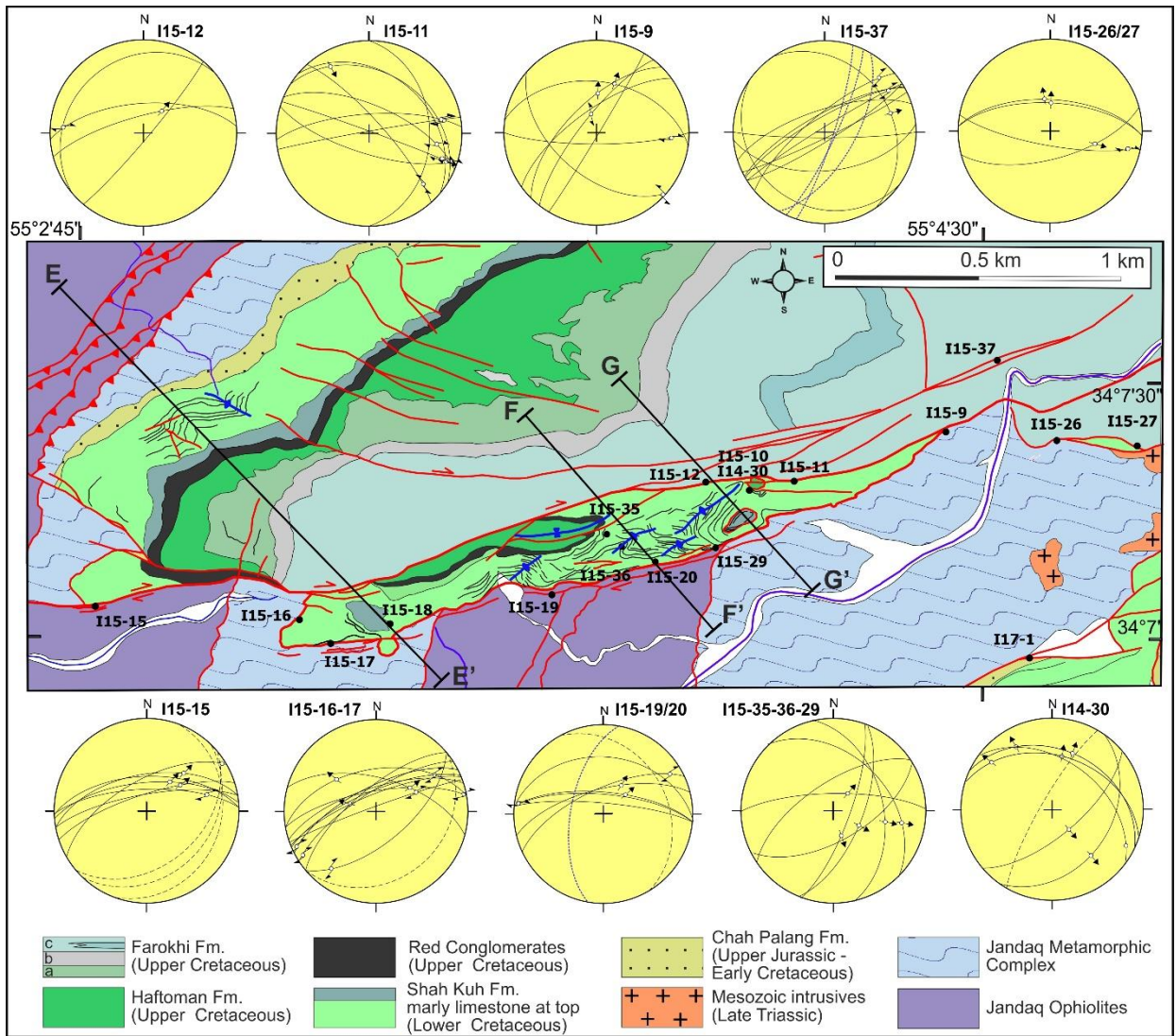
1024

1025

1026

1027

Figure 5. (a) Geological map of the eastern branch of the Arusan Fault; the map is based on our original structural and stratigraphic analyses. We also used ASTER satellite imagery and it was drawn in Google Map. Location of the structural observations and the traces of cross sections are reported. Stereographic projections are Schmidt, lower hemisphere; faults are shown as cyclographic projections with striations and sense of motion when available; blue dotted lines are cleavage and black dotted lines represent bedding. (b) Three plots showing data located out of the map to the south showing faults measured along the Eastern Arusan Fault; location in Figure 11. ThS: Thrust Sheet.

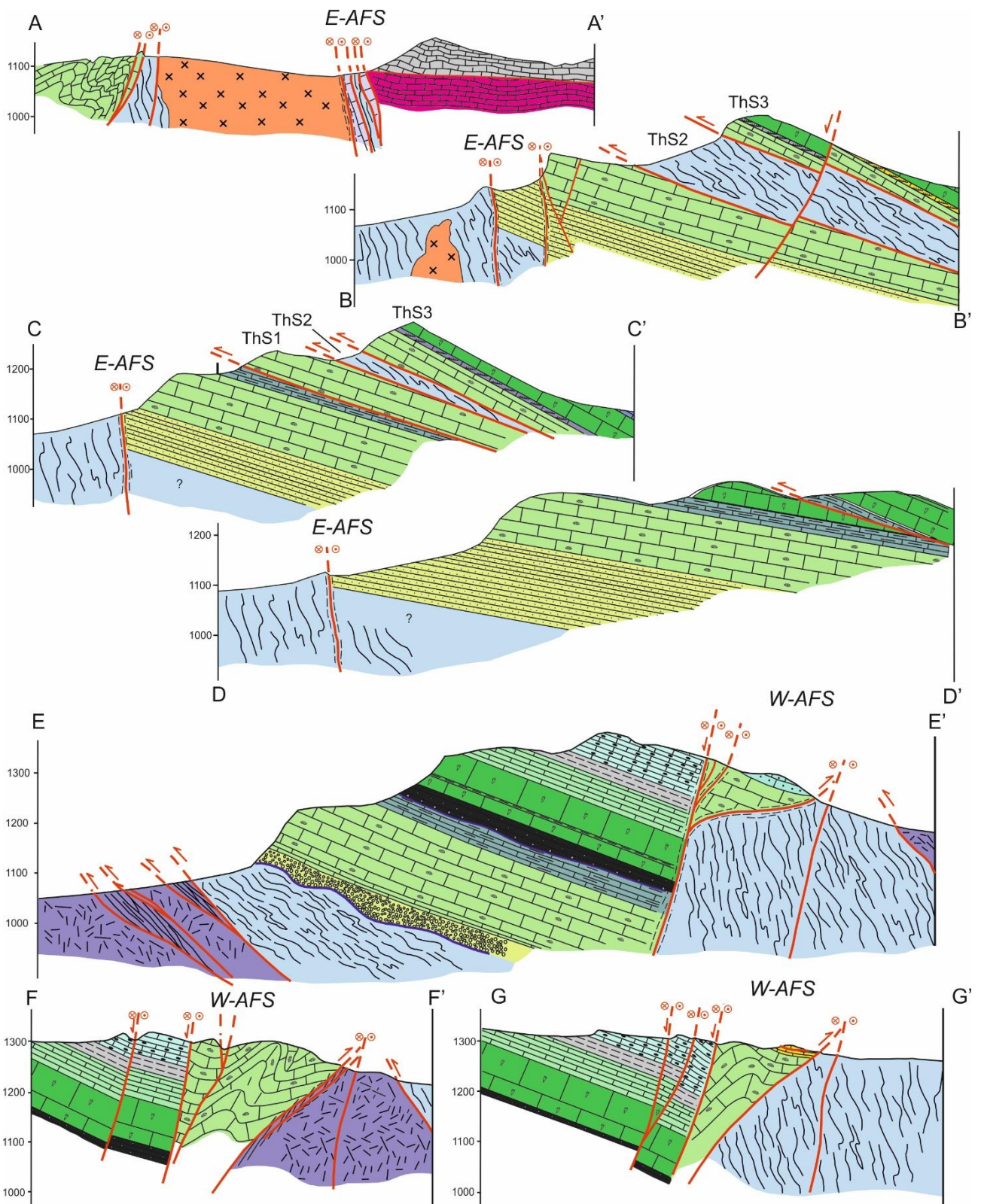


1028

1029

1030

Figure 6. Geological map of the western branch of the Arusan Fault. Symbols as in Figure 5.



1031

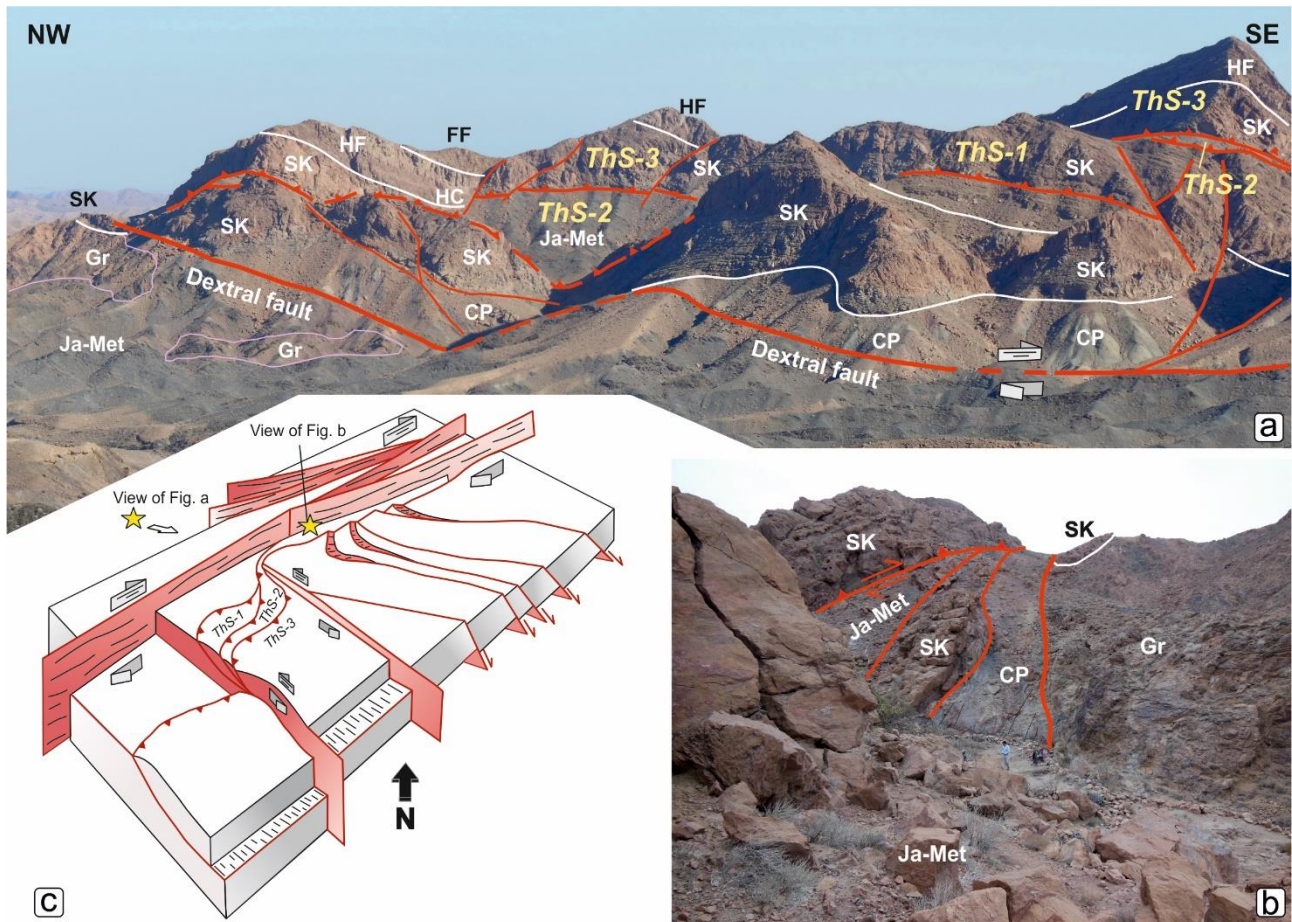
1032

1033

1034

1035

Figure 7. Serial geological sections across the two branches of the Arusan Fault System. Traces of sections A to D are reported in Figure 5; traces of sections E to G are shown in Figure 6. E-AFS: Eastern Arusan Fault System; W-AFS: Western Arusan Fault System; ThS: Thrust Sheet.



1036

1037

1038

1039

1040

1041

1042

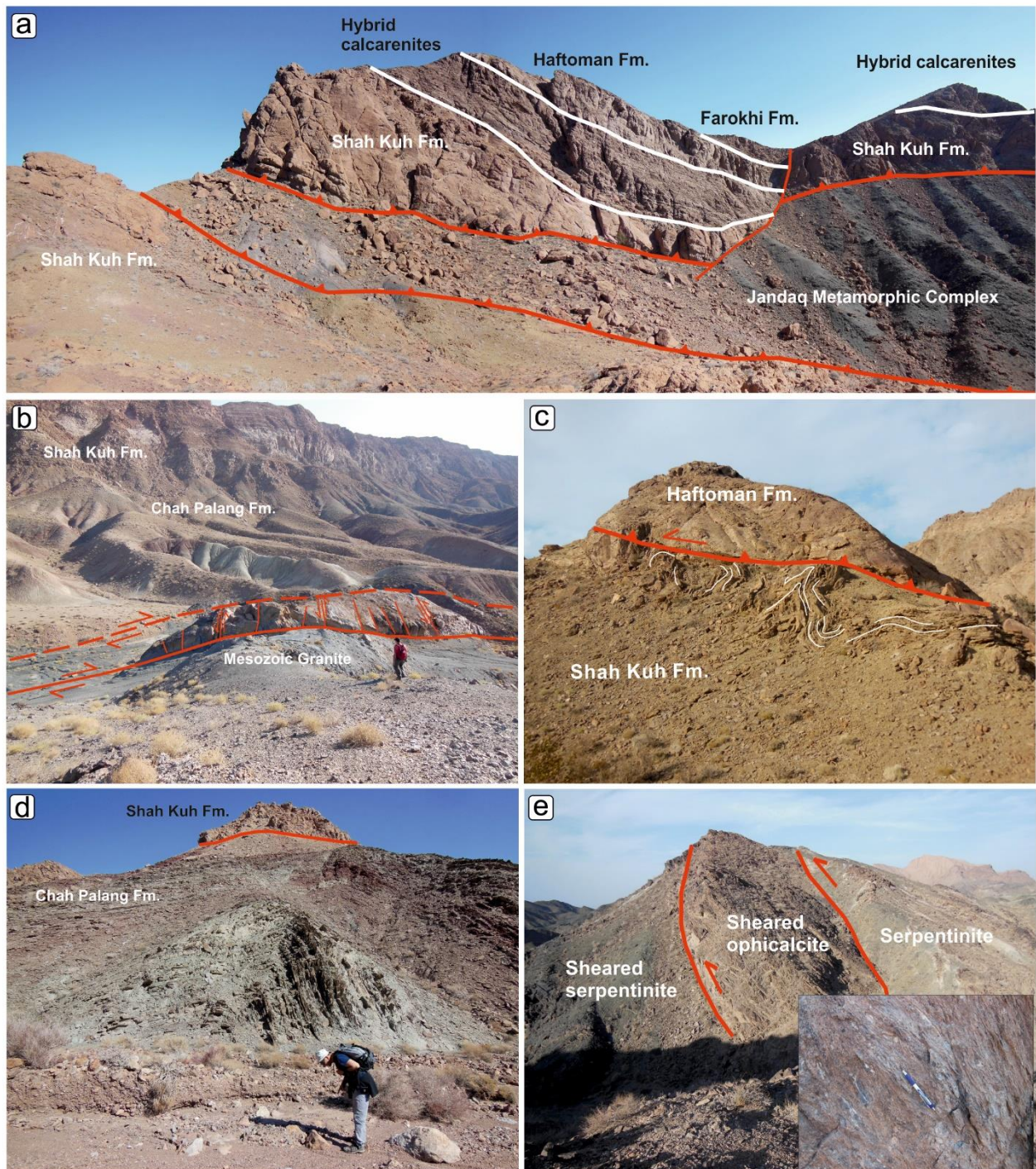
1043

1044

1045

Figure 8. (a) Panoramic view from SSW to NNE of the eastern branch of the AFS, showing field relationships among thrust and strike-slip faults deforming the Cretaceous succession south of Arusan. Gr: Mesozoic granitoids, other symbols as in previous figures. (b) The eastern branch of the AFS south of Arusan, where it shows a marked transpressional character showing high-angle reverse oblique faults including several horses. (c) Schematic block diagram showing geometrical relationships among the western branch of the AFS south of Arusan shown in Figure 8A.

CP: Chah Palang Fm.; FF: Farokhi Fm.; Gr: granites; HC: conglomerates at the base of Haftoman Fm.; HF: Haftoman Fm.; Ja-Met: Jandaq Metamorphic Complex; SK: Shah Kuh; ThS: Thrust Sheet.



1046

1047

1048

1049

1050

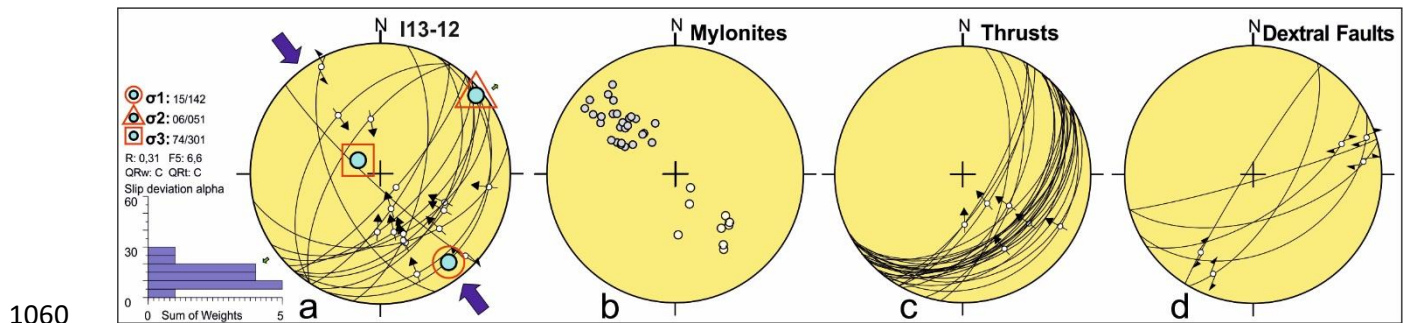
1051

1052

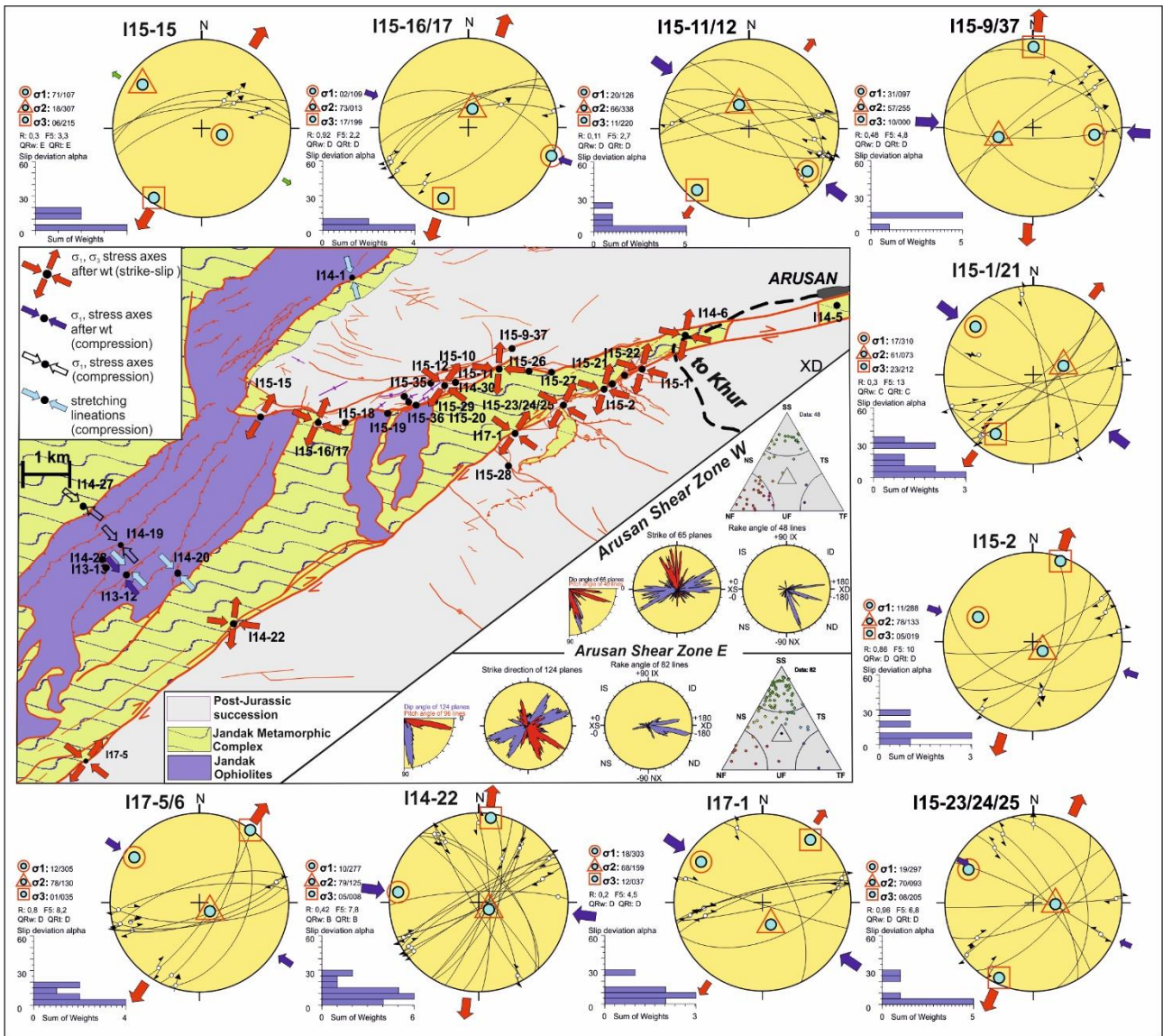
1053

Figure 9. Field photos of the Arusan area. (a) One of the main thrusts displacing the Cretaceous successions and the metamorphic basement. Notice that the Haftoman Formation directly cover the Shah Kuh carbonates. (b) The Western branch of the AFS at site I14-22. The fault juxtaposes Mesozoic pinkish granitoids to the Chah Palang Formation. The Cretaceous succession is exposed on top of the Chah Palang sandstones. Secondary left-lateral faults (Riedel R1) occur between the two main dextral faults. (c) A small klippe consisting of bioclastic limestones of the Haftoman Formation overthrusting folded hybrid limestones of the Shah Kuh Formation along the western branch of the

1054 AFS at site I15-10. (d) Asymmetric closed fold in the Chah Palang sandstones along the Arusan Fault
 1055 System close to the Naqi spring (Figure 3). The Shah Kuh Formation forms a klippe on top of the
 1056 folded sandstones; M. Mattei for scale. (e) Sheared ophicalcite layers about 20 meters thick between
 1057 imbricated ophiolites here consisting of serpentinites, NW of site I14-22 (Figure 3). The inset shows
 1058 the ductile fabric developed along the shear zone within the ophicalcites.
 1059



1061 **Figure 10.** Mesoscopic observation within the Arusan basement consisting of ophiolites and quartzite
 1062 mica schists. (a) Fault associations representing the oldest stage of NW-SE compression with faults
 1063 measured within ophiolite thrust sheets. (b) Poles to mylonitic foliations (grey dots) and extensional
 1064 lineations (empty dots) measured along ductile shear zone preceding the activation of faults,
 1065 measured in the ophiolites. (c) The main thrust fault measured within the Arusan basement. (d)
 1066 Dextral faults crosscutting thrust faults within the Arusan basement.



1067

1068

1069

1070

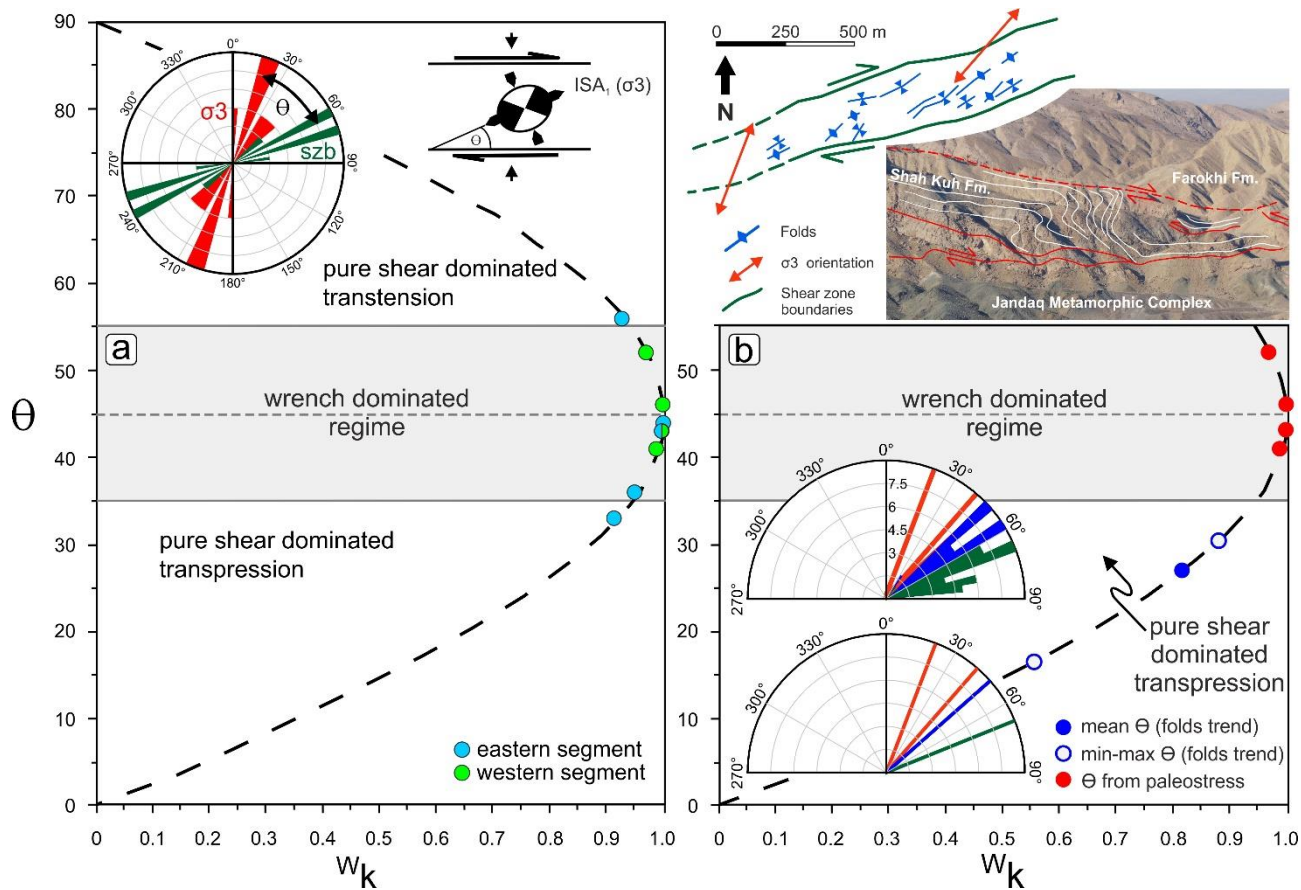
1071

1072

1073

1074

Figure 11. Paleostress reconstruction along the two main branches of the AFS. Obtained paleostress solutions are reported for each site with trend and plunge of the mains stress axes and other significant parameters, including histograms of the angular deviations alpha. See text and table 1 for additional information. Rose diagrams relative to each branch of the fault system are reported; rose diagrams represent strike (blue), dip direction (blue), dip (blue), pitch (red) and rake, with number of analysed faults. Triangular Frolich diagrams are also shown. Stereoplots, rose and Frolich diagrams were obtained with Wintensor (Delvaux & Sperner, 2013, release 5.8.9).



1075

1076

1077

1078

1079

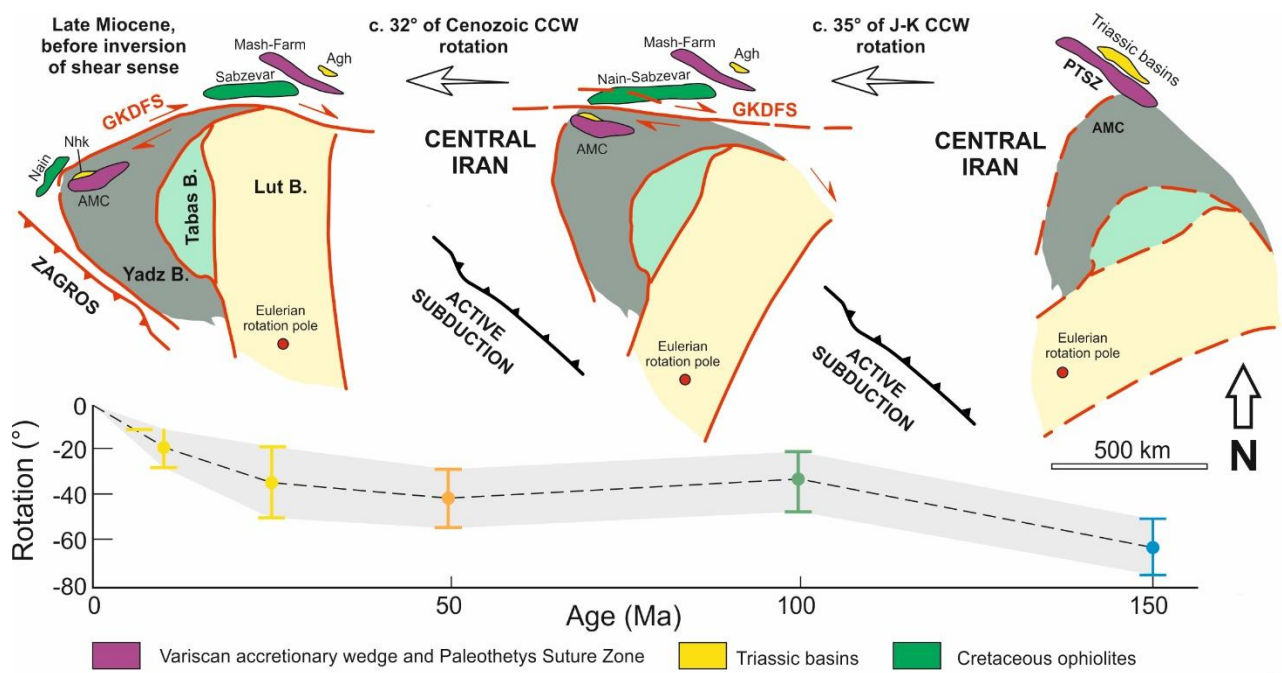
1080

1081

1082

1083

Figure 12. Relationship between the orientation of the maximum Instantaneous Stretching Axis (ISAm_{ax}) with respect to the shear zone boundary (angle θ) related to the kinematic vorticity number W_k (modified after Fossen et al. 1994; Fossen & Cavalcante, 2017). The W_k (a) has been obtained for the Arusan Western Segment shear zone (green dots) and Arusan Eastern Segment shear zone (light blue dots) and (b) for *en échelon* folds occurring in the Arusan Western Fault shear zone. In A are reported a rose diagram showing the value of θ and a schematic representation of the orientation of the ISAs. A scheme showing the shear zone boundaries, σ_3 orientation and the traces of fold axial planes is also reported. szb: shear zone boundaries.



1084

1085

1086

1087

1088

1089

Figure 13. Two stage CCW rotation model of blocks forming the present day CEIM. A pre Late Miocene total CCW rotation (data from Mattei et al., 2015) of 65-70° accounts for the observed displacement of the previously continuous Paleothetys Suture Zone (PTSZ) in NE Iran, as well of the ca. 30° CCW rotation along the precursor of the Great Kavir Doruneh Fault System that displaced the Nain ophiolites from the Sabzevar complex.